Human Molecular Genetics, 2015, Vol. 24, No. 2 **540–558**
doi:10.1093/hmg/ddu475
Advance Access published on September 17, 2014

Comprehensive phosphoproteome analysis unravels the core signaling network that initiates the earliest synapse pathology in preclinical Alzheimer's disease brain

Kazuhiko Tagawa[1,†], Hidenori Homma[1,†], Ayumu Saito[2,†], Kyota Fujita[1], Xigui Chen[1], Seiya Imoto[2], Tsutomu Oka[1], Hikaru Ito[1], Kazumi Motoki[1], Chisato Yoshida[1], Hiroyuki Hatsuta[3], Shigeo Murayama[3], Takeshi Iwatsubo[4], Satoru Miyano[2] and Hitoshi Okazawa[1,*]

[1]Department of Neuropathology, Medical Research Institute and Center for Brain Integration Research, Tokyo Medical and Dental University, 1-5-45, Yushima, Bunkyo-ku, Tokyo 113-8510, Japan, [2]Laboratory of DNA Information Analysis, Human Genome Center, Institute of Medical Science, The University of Tokyo, 4-6-1, Shirokanedai, Minato-ku, Tokyo 108-8639, Japan, [3]Department of Neuropathology, Brain Bank for Aging Research, Tokyo Metropolitan Institute of Gerontology, 35-2, Sakae-cho, Itabashi-ku, Tokyo 173-0015, Japan and [4]Department of Neuropathology, Graduate School of Medicine, The University of Tokyo, 7-3-1, Hongo, Bunkyo-ku, Tokyo 113-0033, Japan

Received August 4, 2014; Revised and Accepted September 9, 2014

Using a high-end mass spectrometry, we screened phosphoproteins and phosphopeptides in four types of Alzheimer's disease (AD) mouse models and human AD postmortem brains. We identified commonly changed phosphoproteins in multiple models and also determined phosphoproteins related to initiation of amyloid beta (Aβ) deposition in the mouse brain. After confirming these proteins were also changed in and human AD brains, we put the proteins on experimentally verified protein–protein interaction databases. Surprisingly, most of the core phosphoproteins were directly connected, and they formed a functional network linked to synaptic spine formation. The change of the core network started at a preclinical stage even before histological Aβ deposition. Systems biology analyses suggested that phosphorylation of myristoylated alanine-rich C-kinase substrate (MARCKS) by overactivated kinases including protein kinases C and calmodulin-dependent kinases initiates synapse pathology. Two-photon microscopic observation revealed recovery of abnormal spine formation in the AD model mice by targeting a core protein MARCKS or by inhibiting candidate kinases, supporting our hypothesis formulated based on phosphoproteome analysis.

INTRODUCTION

Protein phosphorylation is generally accepted as a critical step in the induction or modification of the pathology of neurodegenerative disorders. In Alzheimer's disease (AD) in particular, phosphorylated tau is a critical component of paired helical filaments (PHFs) (1–3) which are the common pathological hallmark of AD and tau-associated frontotemporal lobar degeneration (FTLD). The process might be mediated by various serine/threonine kinases, such as GSK3beta, JNK, PKA, Cdk5 and casein kinase II (CSKII) (4–10), and accelerate the aggregation of tau into PHFs. Physiologically, phosphorylation reduces the affinity of tau to α-tubulin as MAP (11,12) and destabilizes microtubules (13). Hence, hyperphosphorylation of tau might also contribute to the impaired neurites observed in the AD brain (14). Recent results obtained using tau knockout mice showed that tau depletion ameliorated amyloid beta (Aβ) toxicity regarding synaptic function and behavior in AD model

*To whom correspondence should be addressed. Tel: +81 358035847; Fax: +81 358035847; Email: okazawa-tky@umin.ac.jp; okazawa.npat@mri.tmd.ac.jp
†These authors are co-first authors.

mice (15); this supported the updated amyloid cascade hypothesis, which states that soluble amyloid oligomers trigger tau phosphorylation/aggregation and lead to neuronal dysfunction/ cell death (16).

Conversely, from the perspective of signaling networks and of their cross-talk, our understanding of the abnormal phosphorylation signaling observed in the AD brain, including the activities of the kinases mentioned above and the connection between amyloid and tau pathology, is definitely insufficient. In this study, we used high-end screening of phosphoproteins and analyzed the phosphoproteome in the brains of patients with AD, four types of AD mouse models, and one tauopathy mouse model. The vast changes in the phosphoproteome observed were analyzed using a super computer and methods of systems biology.

Finally, we identified the core signaling network shared by multiple mouse models and human patients, which was closely linked to a specific synaptic function. We identified that phosphorylation of myristoylated alanine-rich C-kinase substrate (MARCKS) by overactivated kinases is an initial event to trigger synapse pathology at the earliest stage of mouse AD pathology far before clinical onset and even before histological Aβ deposition. Two-photon microscopy analyses revealed that genetic and pharmacological manipulations targeting MRACKS and candidate kinases recover the loss of spines *in vivo* in the severest AD mouse model, verifying the molecular event triggering synapse pathology that would lead to subsequent pathological abnormalities in AD model mouse brains.

RESULTS

Identification of abnormal phosphoproteins in AD mouse models

The most significant obstacles to phosphoproteomics using human postmortem brain samples are postmortem changes in protein phosphorylation. Previously, we performed proteome-wide analyses of phosphoproteins in mouse brains that had been kept at room temperature or 4°C for different lengths of time (17), to determine the time limitation of human postmortem brains, and found surprisingly diverse changes in phosphoproteins, especially after 12 h (17). This result clearly indicates a risk in performing proteome analyses based solely on human samples. Hence, we used a step-wise approach from AD model mice to AD patient brain samples. We performed phosphoproteome analyses using fresh brain samples (deep frozen immediately, within 5 min after death) from APP-Tg2576 (KM670/671NL), PS1-dE9 (Exon9-deleted), PS2-M1 (N141I) and 5xFAD (APP<KM670/671NL, I716V, V717I> + PS1< M146L, L286V>). In parallel, we performed analysis of Tau (P301S) transgenic mice, as a reference.

Preliminary trials using an AB SCIEX Triple TOF 5600 mass spectrometer were repeated to determine the best conditions for the detection of the highest number of phosphoproteins. A multistep fractionation of samples using cation exchange and reverse-phase columns, the merging of data from multiple analyses of the same sample, and the identification of the appropriate volume and run time for mass spectroscopy allowed us to finally obtain extremely high detection scores (proteins: 2256 with 95% fidelity; peptides: 110632 with 95% fidelity; proteins: 2541 with 66% fidelity; peptides: 117451 with 66% fidelity), which were superior to the scores provided by the company. The number of unique proteins and unique peptides were 2256 and 13644 at 95% fidelity or 2541 and 17211 at 66% fidelity.

Using this condition, first we performed a phosphoproteome analysis on AD mouse models. The mice were dissected at 1, 3 and 6 months of age (4, 12 and 24 weeks). The cerebral cortex, hippocampus and striatum were rapidly divided under a microscope and immediately frozen, although only cortex tissues were used for this study. The whole procedure was completed within 5 min, as assessed using a stopwatch. The background of APP-Tg2576 and 5xFAD mice was C57BL6/SJL, that of PS1-dE9 and PS2-M1 was C57BL6 and that of Tau was C57BL6/C3H. Phosphoproteins were purified from brain samples of five types of transgenic mice and their three background mice using the Titansphere® Phos-TiO kit, labeled with eight different probes using the iTRAQ reagent, and analyzed in one run of mass spectrometry.

The number of phosphoproteins and phosphopeptides identified in the mixed sample of seven mice is listed in Supplementary Material, Table S1. Systems biology analyses were based on 744–1128 unique phosphoproteins identified with 95% confidence and 1799–3477 unique phosphopeptides also with 95% confidence. Using the super computer available at the University of Tokyo, the proteins identified in the nine mass spectrometry analyses were mapped on the integrated protein–protein interaction (PPI) database supplied by the Genome Network Platform of the National Institute of Genetics (http://genomenetwork.nig.ac.jp/index_e.html), which includes the experimentally supported PPI database of the Human Genome Project (GNP) and databases from BIND (http://www.bind.ca/), BioGrid (http://www.thebiogrid.org/), HPRD (http://www.hprd.org/), IntAct (http://www.ebi.ac.uk/intact/site/index.jsf) and MINT (http://mint.bio.uniroma2.it/mint/Welcome.do). The mapped phosphoproteins were designated as 'nodes'. Proteins that were linked directly to the significantly changed phosphoproteins were also attached as 'accessory nodes', and the links between proteins were termed 'edges'. Conversely, proteins that were linked indirectly to the identified proteins via two or more edges were excluded from the network. This network was termed 'mouse default network' (Supplementary Material, Fig. S1a).

Although a single protein had multiple *P*-values of multiple peptides derived from the protein, we integrated the *P*-values using the normal inversion method, and used the integrated *P*-value in the comparison between the model mouse group and the control mouse group. Phosphoproteins that were changed in four types of AD model mice compared with their controls ($P < 0.05$) at any time point between 1 and 6 months were selected as nodes, and their accessory nodes were used for further analyses of the AD-mouse basal network (Supplementary Material, Fig. S1B). The categorization of the phosphoproteins that were changed in the four types of AD mice according to their functions using the protein analysis through evolutionary relationships (PANTHER) classification system (18) (http://www.pantherdb.org/tools/genexAnalysis.jsp) revealed changes in some functional protein groups (Supplementary Material, Fig. S1C). In particular, statistically significant increases were found in structural molecule, cytoskeletal protein binding, enzyme regulator and transmembrane transporter (Supplementary Material, Fig. S1C). In each AD model and at each time point, we drew networks using the significantly changed phosphoproteins as nodes (Fig. 1A; Supplementary Material).

Identification of core phosphoproteins in AD models

In order to identify common changes across four AD mouse models in protein phosphorylation signaling, we employed two approaches (Fig. 1B). The first one was hypothesis-free approach based on simple comparison of phosphoproteome data from multiple mouse models at the same time point. The second approach was Aβ aggregation-linked approach, in which we assumed that amyloid aggregation or a certain process preceding aggregation should trigger abnormal phosphorylation signals. As shown in the figure, the two approaches finally deduced highly homologous phosphoproteins and signaling networks. We then reevaluate the selected phosphoproteins through comparison with the data from human AD brains and from the tau model mice (Fig. 1B).

For the first approach, the nodes of these networks were compared with extract the common phosphoproteomics changes shared by the different models (Supplementary Material, Fig. S2a and Table S2, list of phosphoproteins of A2). The number of common nodes in the intersection group decreased with the increase in the number of AD networks compared (Supplementary Material, Fig. S2a and Table S2, list of phosphoproteins of A3). The intersection of the four AD models included only one node (MAP1B) at 1 month, but did not include any nodes at 3 or 6 months (Supplementary Material, Fig. S2a and Table S2, list of phosphoproteins of A4). Therefore, we selected 65 nodes that changed in two AD mouse models at one or more times, for further analyses (Supplementary Material, Fig. S2A). Among 65 proteins, 51 proteins were detected in a single combination of AD model mice at a single time point, while 14 proteins were found in multiple combinations or multiple time points (Supplementary Material, Fig. S2A). We determined the 14 proteins as the core phosphoproteins selected by hypothesis-free approach.

For the second approach, we performed immunohistochemistry of the four AD mouse models under the exactly same conditions and confirmed the pathological differences among the mouse models (Supplementary Material, Fig. S3). As shown, amyloid deposition was detected in 5xFAD and APP mice starting at 3 and 6 months, respectively. On the other hand, amyloid deposition was not observed in PS1 or PS2 mice until 6 months (Supplementary Material, Fig. S3). Furthermore, tau phosphorylation was not detected in any AD model by immunohistochemistry with AT-8 antibody while it was observed in the tau mouse at 6 months (Supplementary Material, Fig. S3). Phosphorylated tau did not form neurofibrillary tangles, although these structures are a hallmark in the human AD brain. These findings were consistent with those of previous reports.

We therefore hypothesized that 5xFAD and APP mice should share the common pathological signaling at Aβ-starting stage. Hence, we compared significantly changed phosphoproteins between 5xFAD mice at 1 month and APP mice at 3 months or between 5xFAD mice at 3 months and APP mice at 6 months (Fig. 1B; Supplementary Material, Fig. S2B). The comparison deduced 11 common nodes that were shared by 5xFAD and APP mice in relevance to Aβ aggregation in the brain (Fig. 1B; Supplementary Material, Fig. S2B). We determined the 11 proteins as the core phosphoproteins selected by Aβ aggregation-linked approach.

Surprisingly, when we merged the results from different approaches, we found that 8 of the 11 proteins selected by 'Aβ aggregation-linked approach' were also selected by 'hypothesis-free approach' (Fig. 1B and C). Conversely, among 14 proteins selected by 'hypothesis-free approach', more than a half of them were also selected by 'Aβ aggregation-linked approach'. This means that the two independent approaches brought us to the similar conclusion. Together with the idea discussed above, we thereafter focused on 17 proteins as the candidates to compose AD core network.

It is important to note that all the changes in phosphoproteins started before the onset of symptoms (Supplementary Material, Fig. S4). Behavior tests, including the Morris water maze, rotarod, open field, elevated plus maze, light–dark boxes and fear-conditioning tests revealed that the four AD mouse models (PS1, PS2, APP and 5xFAD) did not exhibit a definite onset of the symptoms by 6 months. Therefore, it is possible that this phosphoproteomics study has detected the subset of proteins that participate in the initial stage of mouse AD pathology.

AD core phosphoproteins are shared by tau mouse and human AD

Next, we reexamined the selected proteins from the aspect of the transition from amyloid pathology to tau pathology that is assumed in the amyloid cascade hypothesis. The comparison with the result of tau mice at different time points revealed 10 among 14 phosphoproteins were also changed in tau mice. They were ADDB, NFH, NFL, SPTA2, BASP1, CLH, MARCS, NEUM, SRRM2, and Marcksl1 (Fig. 1C).

Although not included in the 17 proteins, hypothesis-free approach detected tau in 65 proteins (Supplementary Material, Fig. S2A). An increased phosphorylation of tau was shared by severe AD (5xFAD, APP) and tau model mice at 1 month (Supplementary Material, Table S2). Thus, our data supported that tau phosphorylation is a link from amyloid pathology to tau pathology. However, it was unexpected that tau phosphorylation started in the brain of young AD model mice (1 month) far before tau phosphorylation was detected by immunohistochemical analysis (Supplementary Material, Fig. S3) and far before symptoms were detected by behavior tests (Supplementary Material, Fig. S4). It was also unexpected that tau phosphorylation paradoxically disappeared in the AD mouse models after 3 months, with the exception of its reappearance in the 5xFAD mouse at 6 months. It is well known that PHFs (or tangles) are never formed in these AD model mice. Tau phosphorylation may be an early pathological event that started immediately after or almost in parallel with amyloid pathology, whereas additional factors might be necessary for its development to PHF, similar to human AD.

In parallel, we reexamined the 17 proteins selected from AD model mice comparing with the phosphoproteome data from human AD brains. For the purpose, we performed similar mass analyses using five human AD brains. These brain samples were deep frozen within 1 h and their pathological examination excluded contamination with non-AD pathologies, such as Lewy bodies and argyrophilic grains. The preparation time is so far the shortest when we follow legal regulation

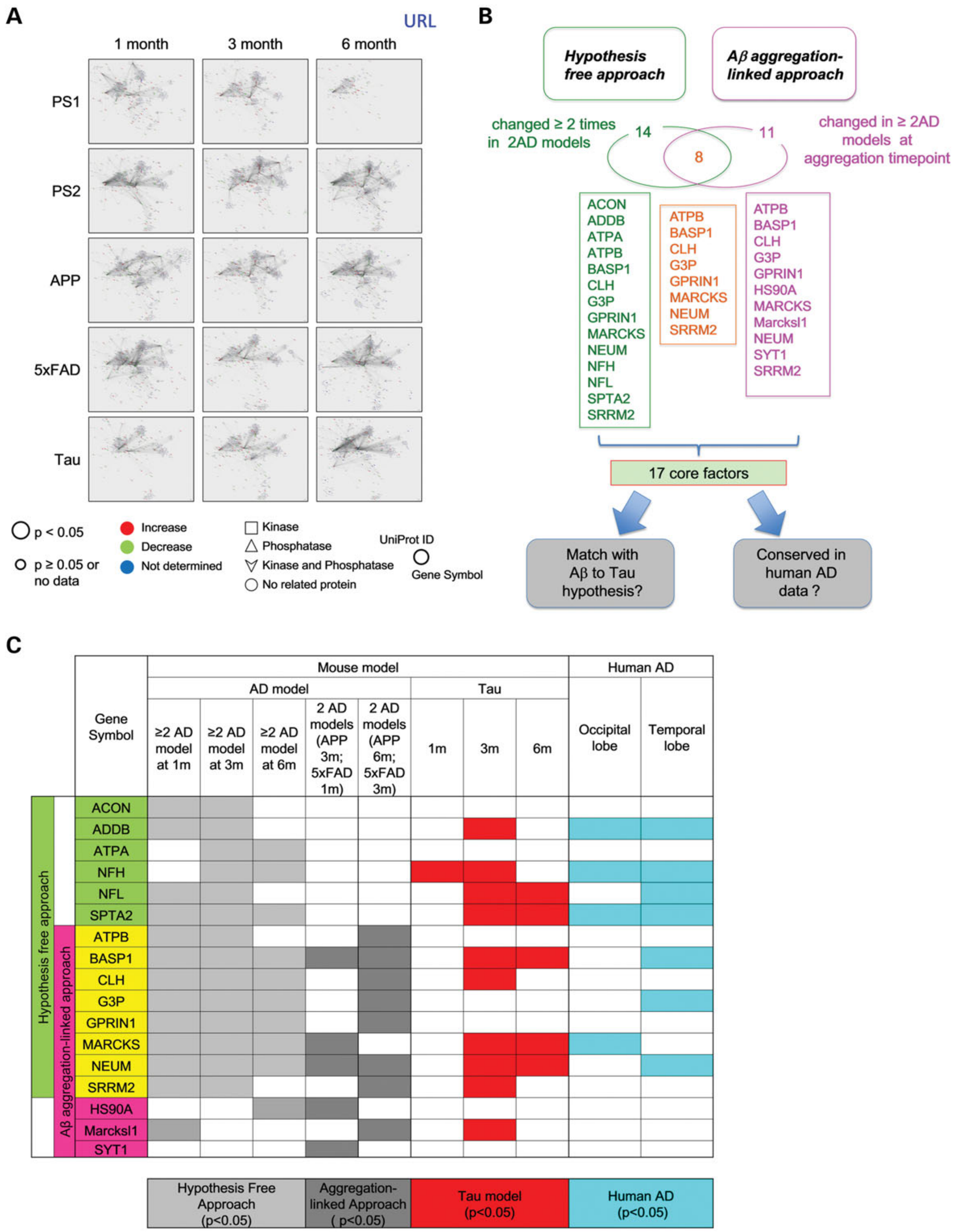

Figure 1. Phosphoproteomics analysis with multiple AD mouse models and selection of core phosphoproteins in AD pathology. (**A**) Phosphoprotein networks were generated using significantly changed phosphoproteins in each AD model at 1, 3 and 6 months of age (large circle, $P < 0.05$, normal inversion method). Accessory proteins within one edge (small circle, $P \geq 0.05$) were also included in the networks. Uniprot ID and gene symbol are indicated at the upper left and lower right of the

in Japan. Temporal lobe (temporal pole) and occipital lobe (occipital pole) samples from five AD brains, five age-matched control brains and five Diffuse Lewy Body's disease brains were used for mass spectrometry. In general, these brain regions were dominantly affected in AD. To keep the purity of AD pathology, we could not increase the sample number anymore even by using Japanese brain bank network that possesses >1000 human AD brains.

Based on the phosphoproteins that were detected in all human brains, we generated a 'human default network' (Supplementary Material, Fig. S5). In this case, however, the edge and accessory nodes were added to the node, not only based on the human PPI database but also on mouse and rat PPI databases, so that comparison between human and mouse networks in the next step did not lead to a loss of important molecules, such as kinases/phosphatases. Phosphoproteins that were changed either in the temporal or occipital lobe of AD brains compared with those of normal or DLB brains, were selected and termed 'human AD—Control nodes' (Supplementary Material, Fig. S6a) and 'human AD—DLB nodes' (Supplementary Material, Fig. S6b), respectively. The detailed quantitative changes of these node phosphoproteins are listed (Supplementary Material, Table S3). Networks based on the human AD—Control nodes in occipital and temporal lobes were generated and used for comparison with the 17 proteins based on the mouse phosphoproteome (Supplementary Material, Fig. S6c). It is of note that all these disease-specific nodes in 'human AD—DLB nodes' were detected in the human AD—Control network (Supplementary Material, Fig. S6a).

Significance of the mouse AD core network proteins was tested by comparison with the human data. The human phosphoproteome data detected changes of ADDB, NFH, NFL, SPTA2, BASP1, G3P, MARCKS and NEUM (Fig. 1C). Their changes were also detected in tau model mice except G3P (Fig. 1C). The two re-examinations with tau mouse and human AD brains strongly supported significance of the AD core phosphoproteins.

AD core network functionally focuses on synapse and energy metabolism

We therefore drew the AD core network with the 17 core phosphoproteins on integrated human–mouse PPI database (Supplementary Material, Fig. S7). The central color of the node indicates whether they were selected by hypothesis-free approach (light green), Aβ aggregation-linked approach (magenta) or both approaches (yellow). The color of circle line surrounding the node indicates whether the change was conserved in tau model mice (red), human AD brain (blue) or both (purple). In the URL, any type of network can be retrieved from the default core network.

Surprisingly, we found that 12 of 17 proteins were directly connected and 3 proteins, SRRM2, BASP1 and ADDB, were linked via one independent protein (Supplementary Material, Fig. S7; Fig. 2). Marcksl1 is highly homologous to MARCKS, though the direct connection was not included in PPI databases. Thus, it was concluded that at least the 15 proteins form a single functional network. More surprisingly, functional annotation of the core phosphoproteins as follows revealed that their functions were directly linked to the synapse functions such as spine formation and energy production (Fig. 2).

SPTA2, a brain alpha-spectrin, is an actin cross-linking protein that is highly expressed in the brain (19). SPTA2 interacts with SHANK1 at the postsynaptic density (20) or with ADDB/adducin-b, which was also identified here as a final node (Fig. 1B and C). SPTA2 and ADDB/adducin-b form spectrin/adducin/actin complexes (21) and are substrates of protein kinase C (PKC). After their phosphorylation, the complex becomes unstable and membrane stability is reduced. ADDB contains a MARCKS-related domain and its phosphorylation by PKC regulates its postsynaptic localization and inhibits actin/spectrin complex formation (22). Intriguingly, this system was recently shown to control synapse elaboration and elimination, although the results were based on the neuromuscular junction in *Drosophila* (23).

MARCKS, BASP1 and NEUM are heavily involved in lipid-raft-originating signals. MARCKS is a specific substrate of PKC, which is located at the plasma membrane. After phosphorylation or binding to calmodulin, it is released from the plasma membrane and translocated to the cytoplasm, where it inhibits F-actin cross-linking (24). A mouse carrying mutant MARCKS showed various morphological and functional abnormalities of the brain (25). MRP/Marcksl1 is another member of MARCKS family, which is involved in PKC signaling. In addition Marcksl1 is phosphorylated by JNK to regulate actin stability and filopodium formation of neurons (26).

NEUM/neuromodulin/GAP43 is a critical component of growth cone/axon presynaptic terminals and a major PKC substrate (27). NEUM interacts with several molecules, such as PIP2 and palmitate, or the cytoskeletal proteins actin, spectrin, synaptophysin and tau. Similar to MARCKS and SPTA2, NEUM is also regulated by calmodulin and shuttles between the membrane and the cytoplasm (28). Therefore, NEUM is an adaptor protein that regulates presynaptic terminal functions via cytoskeletal modulation. As expected, NEUM is involved in memory and LTP formation (29). BASP1/NAP-22/CAP23 is a PEST-motif-containing myristoylated protein that is abundant in axonal terminals (30). Although its function has not been well characterized, it exists at the inner surface of lipid rafts in the plasma membrane. In addition, BASP1, MARCKS and NEUM seem to modulate PI(4,5)P2 via a common mechanism (31). The phosphorylation-dependent interaction between BASP1, MARCKS or NEUM and calmodulin promotes the formation of the actin network (31). Collectively, these members of the AD core proteins seemed to form networks that regulate pre- and post-synapse morphologies.

Although phosphoproteomic changes of SYT1/synaptotagmin1 and GPRIN1/G-protein-regulated inducer of neurite outgrowth-1 were confirmed neither in tau mouse nor human AD brains, these proteins might also play a role in the early stage AD or

node, respectively. (**B**) Strategies to select core phosphoproteins. Hypothesis free approach was the selection based on commonality in multiple AD models irrespective of the severity or the Aβ aggregation property. Aβ aggregation-linked approach was the selection of common proteins shared by two AD models (APP and 5xFAD) at the time point just before or just after initiation of Aβ deposition in the histological analysis. The number of selected phosphoproteins by each approach and their names are listed. (**C**) List of 17 core phosphoproteins and their changes in AD model, tau model and human AD brains. Proteins selected from hypothesis-free approach, aggregation-linked approach and both approaches were shown in different colors.

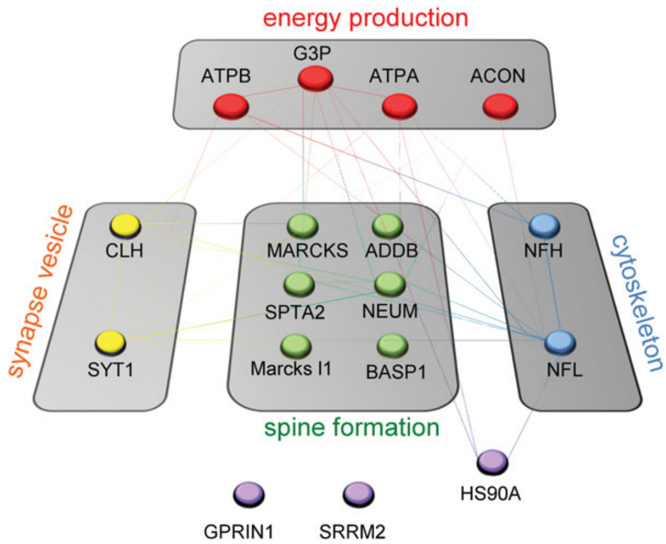

Figure 2. AD core phosphoproteins compose a directly connected network. AD core phosphorpoteins were grouped based on their functions, and direct interactions among the core proteins were indicated with edges. When the core proteins were linked via one protein, such proteins (14-3-3 and PKC) are also shown in the network.

mAD pathology. Especially, SYT1/synaptotagmin1 could be important, because it controls vesicle recycling at synapse terminal making a complex with a vesicle cargo molecule CLH/clathrin heavy chain (32), which was also selected both by hypothesis-free and Aβ aggregation-linked approaches.

Interestingly, molecules involved in energy production were also selected. ATPA and ATPB are mitochondrial ATP synthetase subunit A and B, respectively. ACON is mitochondrial aconitase 2 that catalyzes isomerization of citrate in TCA cycle. G3P/GAPDH/glyceraldehyde-3-phosphate dehydrogenase is the critical enzyme in glycolysis, but it also plays nuclear functions through the nitrosylase activity, and affects assembly of microtubules via the same mechanism. Thus G3P might be also related to cytoskeleton and the classification was tentative for this protein (Fig. 2).

There remained some proteins that could not be exactly categorized. GPRIN1/G protein-regulated inducer of neurite outgrowth 1, an effecter of Gαo enriched in the growth cone membrane fraction that induces neurite outgrowth (33) but the detailed functions have not been clarified. PPI databases did not support interaction with other core proteins. Thus, GPRIN was not included in spine formation domain in Figure 3B, tentatively (Fig. 2). SRRM2/SRm300/serine–arginine repetitive matrix protein 2, which is involved in splicing with SRm160 (34), was functionally isolated from the other core network proteins (Fig. 2). HS90A/HSP90, a molecular chaperon involved in protein folding and quality control of many client proteins, was linked to multiple proteins in the core network because of its general functions.

These reviews of previously published results further support our idea that the early phosphoproteomic changes in the AD pathology are selectively focused on a few networks that regulates synaptic function and energy metabolism (Supplementary Material, Fig. S8).

Dynamic changes of phosphoproteins before the symptomatic onset

In addition to the early changes in phosphorylation of synapse-related molecules before the onset, the second important finding in this study was that their changes were not stable but dynamic during disease progression. Given that the patterns of chronological changes in the core phosphoproteins were quite complex, we analyzed them by multiple bioinformatics methods.

First, we tested the consistency of pathological changes in the core phosphoproteins at 3 and 6 months in comparison to the baseline at 1 month. In this hypothetical model, disease-related changes should occur from 1 to 3 months and should sustain from 3 to 6 months. One, 3 and 6 m values were calculated as the ratio of the quantity of phosphoprotein in an AD model mouse to that in the background mouse, and the relative change of 3 m/1 m and 6 m/1 m were calculated. We plotted the relative changes on the coordinate plane (Supplementary Material, Fig. S9A). The x-axis is set as the 3 m/1 m and the y-axis is set as the 6 m/1 m. The coordinate plane is formed by these axes intersecting at the value of 1 because the coordinates mean that there is no change in the ratio from the time point of 1 month. In order to know the background changes, we similarly analyzed available 563 phosphoproteins, which had reliable values in all mouse models at all time points (confidence $> 95\%$, $P < 0.05$).

On this coordinate plane, we also defined two parameters, r (distance from the origin) and *theta* (the angle between the line from the origin to the coordinate of a protein and the line from the origin with a slope of 1) for each protein (Supplementary Material, Fig. S9B). The variable r represented the extent of change and *theta* represented the consistency between the change from 3 to 6 months. If *theta* is positive, the phosphoprotein change is a bump pattern. If *theta* is negative, the phosphoprotein change is a dent pattern.

This analysis revealed although r values were variable among core proteins and mouse models, *theta* values were small in all proteins. The result meant that the changing orientation was largely consistent at 3 and 6 months in all core phosphoproteins (except HS90A) despite of variable extents of the changes.

We next performed cluster analyses (Supplementary Material, Fig. S9c) to elucidate more detailed changing patterns of the core phosphoproteins in multiple AD mouse models. We analyzed information of four mouse models at three time points (12 dimensions) by the Ward's method (35), and classified the 17 core phosphoproteins and other control phosphoproteins. As expected the core proteins were clustered into several groups (Supplementary Material, Fig. S9c), reflecting the chronological patterns of phosphoproteins (Supplementary Material, Fig. S9A and B).

Aging-related changes of phosphorylation at peptide and protein levels in AD mouse models and background mice

Moreover, we asked the difference in age-related changes of the core phosphoproteins between a single AD model and control mice. For this purpose, we performed again mass analyses with three sets of new samples including 5xFAD and background mice at multiple time points from 1 month to 12 months. Using

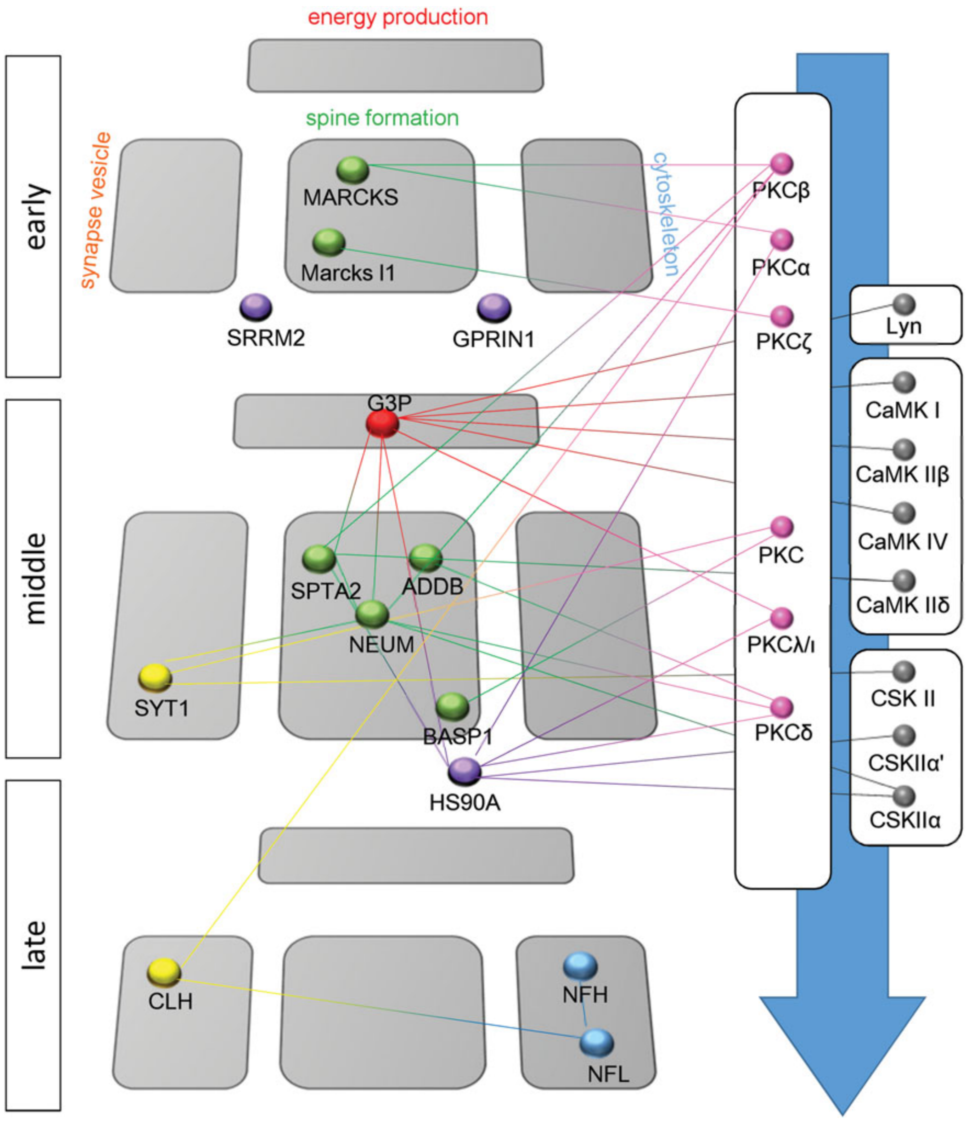

Figure 3. Dynamic changes of AD core network during pathological progression. Relationship between core phosphoproteins and responsible kinases are schematically presented according to the chronological progression of AD pathology based on 5xFAD mice. Amyloid deposition in the hippocampus starts at 3 months in this model but the deposition was not detected in the cortex used for two-photon microscopic analysis. Early, middle, late correspond to 1, 3 and 6 months, respectively.

the data, we calculated the values of 5xFAD and background mice corrected by the value of background mice at 1 month, and plotted on the graph to explore the changes of the core proteins (Supplementary Material, Fig. S9D and Table S4). By this method, we expected to differentiate pathological aging of AD from normal aging in phosphoproteome.

In most of the core phosphoproteins, comparison of integrated value of protein phosphorylation of 5xFAD and background mice from 1 to 12 months with the value of background mice at 1 month revealed that the patterns of change are qualitatively similar in normal and pathological aging in most cases (Supplementary Material, Fig. S9e and Table S4). Comparison of integrated protein phosphorylation values between 5xFAD and background mice at each time point revealed that in most cases the extent of pattern-specific phosphorylation was more prominent in 5xFAD mice (Supplementary Material, Fig. 9f and Table S4).

Phosphorylated MARCKS, Marcksl1 and SRRM2 were decreased during physiological aging. These phosphoproteins were increased at 1 month in 5xFAD mice in comparison to the background mice, but the difference diminished during the timecourse (Supplementary Material, Fig. S9e, early). In these proteins, quantitative difference of phosphorylation between 5xFAD and background mice was remarkable at 1 month (Supplementary Material, Fig. S9f, early). Phosphorylated SPTA2 and G3P increased during physiological aging, while phosphorylated ADDB, SYT1, BASP1 and HS90A had a peak at 3 or 6 months. These phosphoproteins increased in 5xFAD mice at 3 months then decreased faster than in the background mice (Supplementary Material, Fig. S9e). NEUM decreased during physiological aging but similar higher in 5xFAD mice at 3 months (Supplementary Material, Fig. S9e) and the difference between 5xFAD and background mice followed the pattern (Supplementary Material, Fig. S9f). Interestingly, phosphorylated SPTA2, G3P and SYT1 were markedly lower in 5xFAD mice than in the background mice at 1 month but the relationship was reversed at 3 months (Supplementary Material, Fig. S9E and F).

Moreover, we extended the analysis of chronological change in phosphorylation to that of each phospho-site at the phosphopeptide level in four AD mouse models.

In this case, we revisited all phosphopeptide data of 17 core proteins (Fig. 1C) and examined how each phosphopeptides were chronologically changed in four AD mouse models and background mice (Supplementary Material, Fig. S9G, H and Table S5). Similarly to the analysis of protein phosphorylation (Supplementary Material, Fig. S9E), we first investigated how each phosphopeptide was changed from the value of background mice at 1 month in four AD models and in background mice (Supplementary Material, Fig. S9G). We found the most of the phospho-sites in MARCKS, Marcksl1 and SRRM2 showed the similar patterns to that of integrated protein phosphorylation (Supplementary Material, Fig. S9G). Moreover, the early changing pattern was shared across four AD mouse models at most of phospho-sites in MARCKS, Marcksl1 and SRRM2 (Supplementary Material, Fig. S9G, marked magenta). These findings were basically reconfirmed in comparison of the phosphopeptide quantities of AD models with that of background mice at each time point (Supplementary Material, Fig. S9H). Intriguingly, the chronological pattern of the three proteins was shared by multiple phospho-sites across genotypes (Supplementary Material, Fig. S9G and H).

In GPRIN1, chronological patterns seemed similar across genotypes in phosphoprotein and phosphopeptide analyses. However, phosphorylation levels were nearly normal at 1 month and they went down to hypophosphorylated states when four AD model mice and background mice became old (Supplementary Material, Fig. S9g and H). As GPRIN1 is a target protein of G-protein signaling for neurite outgrowth (33), the chronological change might be related to the loss of neurite extension during progression of the AD-like pathology and in physiological brain aging. In a part of 'middle pattern proteins' like ADDB, NEUM and BASP1, a part of phospho-sites such as Thr36 and Ser92 of BASP showed constantly the middle pattern across genotypes (Supplementary Material, Fig. S9G and H). In 'late pattern proteins', NFL possessed phospho-sites that were progressively hyperhosphorylated during physiological and pathological aging (Supplementary Material, Fig. S9G and H). We summarized all the actual changes of phosphopeptides in Supplementary Material, Table S5.

Collectively, we performed comprehensive and extensive analyses of phosphoproteins and phosphopeptides according to the work flowchart (Supplementary Material, Fig. S10). All our experiments along the flow chart and the final comparison of protein- and peptide-based results (Supplementary Material, Fig. S11) revealed highly homologous chronological changes of specific proteins including MARCKS, Marcksl1, SRRM2, ADDB, NEUM, BASP1, GPRIN1, NFL, NFH and SYT1. Intriguingly, the chronological patterns of phosphorylation in these proteins were conserved across AD model genotypes, especially in MARCKS, Marcksl1, SRRM2, ADDB, NEUM, BASP1, GPRIN1 and NFL (Supplementary Material, Figs S9 and S11).

The different patterns of phosphorylation among the core proteins might suggest their different roles in the progression of mouse AD pathology. Therefore, we restructured the core phosphoprotein network according to the time point when such an overshoot of protein phosphorylation occurred (Fig. 3). As shown in the figure, MARCKS and its homolog Marcksl1 were changed earliest, and they were connected to the other core phosphoproteins involved in the same functional domain whose phosphorylation changes followed. Thus, among the AD core phosphoproteins related to synapse function, MARCKS and Marcksl1 are the best candidates for the molecules initiating the synapse pathology in phosphorylation signals. Especially, MARCKS was commonly detected as a molecule changed at the early stage by the aggregation-linked approach (Fig. 1C) and by the aging pattern analysis (Supplementary Material, Fig. S9D and E), suggesting that MARCKS is the most reliable candidate for the phosphorylation signal molecule in the early stage of AD pathology. Taken together, we decided to focus on MARCKS in the following experiments.

Identification of kinases that regulate AD core network

Next, we asked which kinase/phosphatase were responsible for the changes in the AD core network. First, we identified kinases and phosphatases among the proteins that were linked directly to the core proteins of the AD core network and listed their names (Supplementary Material, Table S6). When we ranked kinase/phosphatase that modify the core proteins, PKC was identified as the most critical enzyme that could phosphorylate the largest number of core proteins (Supplementary Material, Table S6). MAPK and MAPKKK followed PKC as expected from many previous reports suggesting their roles in AD pathology (Supplementary Material, Table S6). These kinases may be master enzymes that regulate phosphorylation state of the core network proteins.

The second group following the three kinases included CSKII, receptor interacting serine/threonine-protein kinase 1/3, cyclin-dependent kinase 5/6 and protein kinase C-like 1. The third group involved Ca^{2+}/calmodulin-dependent kinase (CaMKI/II), protein kinase D, and so on. In addition, Lck/Yes-related novel protein tyrosine kinase (Lyn) and the other 20 kinases were identified as candidates to regulate the core network, although they were linked to only one protein (Supplementary Material, Table S6).

Comparison between the timecourse result of core phosphoproteins in 5xFAD mice and the result of linked kinases suggested the enzyme−substrate relationship (Fig. 3). The early, middle and late-stage patterns of core phosphoproteins are correlated to PKC, Lyn, CaMK and CASK (Fig. 3). Among them, PKC family kinases seemed activated earliest among various kinases, and the activation sustained to the late stage (Fig. 3). MARCKS and Marcksl 1 were the first targets of PKC, and G3P, NEUM, BASP1 and SPTA2 were the second group (Fig. 3). Consistently, the cluster analysis of core phsophoproteins in multiple AD models showed that chronological changes of G3P, NEUM, BASP1 and SPTA2 were homologous (Supplementary Material, Fig. S9c) and they were linked to PKC (Supplementary Material, Table S6).

We also went back to the phospho-site data of 12 core proteins that were selected through confirmation of peptide-based changes between AD mouse models and background mice (Supplementary Material, Fig. S10). Probability of PKC-mediated phosphorylation of those phospho-sites was estimated by two computer-based analyses, NetworKIN (36) and NetPhosK (37). These analyses strongly suggested that the earliest conserved phosphorylation sites in MARCKS are the target of PKC (Supplementary Material, Table S6) and the other core proteins like GPRIN1, ADDB, BASP1, NEUM and SPTA2 could be phosphorylated by PKC (Supplementary Material, Table S6).

AD core network is active before the onset

Finally, we intended to verify the significance of AD core network in the pathology by *in vivo* and *in vitro* experiments. The functional domains of core factors revealed by our phosphoproteome analysis suggested that specific phosphorylation signals linked to pre- and postsynaptic cytoskeletons are perturbed at the earliest phase of AD (Supplementary Material, Fig. S8). The cytoskeleton network (especially actin-related network) suggested by our results is a key regulator of dendritic spine formation (38,39), and consistently abnormal spine formation has been implicated in AD. Presynaptic facilitation and resulting enhanced spine formation within a short-time range was suspected in the early stage of AD pathology (40). Among the various signaling pathways that have been implicated in such AD pathology, our phosphoproteomics analysis suggests that the links from MARCKS to actin polymerization and from SPTA2 to actin–spectrin cross-linking become abnormal at an early stage of AD, and that these networks are activated rather than repressed. Therefore, we used presymptomatic 5xAD mice (at 12 weeks of age) and analyzed the dendritic spine dynamics via two-photon microscopy (Fig. 4A). Simultaneously, we attempted to recover the spine abnormalities via pharmacological intervention by targeting the kinases or via shRNA-mediated knockdown of the core phosphoproteins identified in this study.

Using two-photon microscopy, we first detected a remarkable decrease in the dendritic spine density of cortical neurons in layer 1 of living 5xFAD mice at 12 weeks (Fig. 4A and B). The number of spines per dendritic shaft length was decreased in all types spines (thin, mushroom and stubby) (Fig. 4C). Regarding absolute numbers of dendritic spine per 100 μm, spine formation, elimination and stable spine were all decreased (Fig. 4D and E, upper panel). Regarding the ratio of the three types of spine dynamics, their formation was decreased, whereas their elimination and stability were not significantly changed in 5xFAD mice (Fig. 4E, lower panel). Collectively, these data suggest that spine formation processes are affected in the pathology of 5xFAD mice. These results were basically consistent with previous findings from AD mouse models (40–42).

Next, we tested the effect of candidate core kinases, which were expected to affect the core network at the early-middle stage (Fig. 3), on the synaptic pathology of 5xAD mice via intrathecal injection of several drugs. After preliminary screening inhibitors and activators of multiple kinases found in this study (Supplementary Material, Table S6), we found that three drugs, a PKC inhibitor (Gö6976, Calbiochem, CA, USA), a Lyn kinase activator (MLR1023, Glixx Laboratories, MA, USA) and CamKII inhibitor (KN-93, Cayman, MI, USA) were effective. Based on previous findings, overactivated PKC at synapses was expected to inhibit actin polymerization and actin–spectrin cross-linking (Supplementary Material, Fig. S8). Non-phosphorylated and phosphorylated CamKII have been also implicated in spine formation. In contrast, the role of Lyn kinase in neuronal synapses has not been investigated. As expected, the PKC inhibitor (Gö6976) ameliorated the spine abnormality observed in 5xFAD mice (Fig. 4A–E), increased total spine density (Fig. 4A and B), and recovered the number of thin, mushroom and stubby types of spine (Fig. 4C). Regarding spine dynamics, Gö6976 increased spine formation and stability in 5xFAD mice (Fig. 4D and E). CamKII inhibitor (KN-93) also showed curative effects on the spine formation and stability, and recovered all types of dendritic spines that had been impaired in 5xFAD mice (Fig. 4D and E). The Lyn kinase activator (MLR-1023), which is also known as an insulin-receptor-potentiating agent (43), played a beneficial role in this case (Fig. 4A–E). The latter finding might be related to the insulin resistance observed in the AD brain (44).

To confirm the effect of kinase intervention *in vivo*, we prepared brain samples after two-photon microscopy observation, and examined the immunoreactivity of activated form of kinases. We found that the tested kinases (PKCβ, PKCδ and CamKII) were actually activated in 5xFAD mice in the cortical area (retrosplenial cortex) where we obtained images, though the immunostain patterns were different among the kinases (Fig. 4F). Quantification of immunostain signals supported the effect of kinase inhibitors (Fig. 4G). We tested multiple commercial anti-Lyn kinase antibodies but they were not sufficient to obtain quantitative data.

Involvement of MARCKS in the AD spine pathology

Further to confirm the target proteins of PKC and CamKII, we knocked down the candidate proteins, MARCKS, the most reliable protein whose phosphorylation was changed at early stage, and SPTA2, a representative phosphoprotein changed at middle stage, by injecting lentiviral vectors expressing their shRNA into the cortex of presymptomatic 5xFAD mice at 12 weeks. Phosphorylated MARCKS by PKC inhibits F-actin cross-linking (24), thus overactivity of phosphorylated MARCKS disturbs recycling of actin filaments and spine formation. SPTA2, a brain alpha-spectrin, is an actin cross-linking protein that is highly expressed in the brain (19). Phosphorylation of spectrin induces the loss of function: its detachment from actin filament (45). Thus, overactivity of phosphorylated SPTA2 leads to the loss of its physiological function to stabilize membrane shape that is essential for the spine formation.

As expected, we found that suppression of MARCKS by shRNA ameliorated the pathological change of spines in 5xFAD mice (Fig. 5A–E). MARCKS-shRNA recovered the decrease of spines (Fig. 5A and B), increased premature and mature spines (Fig. 5C), and improved the spine formation (Fig. 5D and E) in 5xFAD mice at 12 weeks. On the other hand, suppression of SPTA2 could not recover the AD spine pathology (Fig. 5A–E). This had been expected because SPTA2 is a cytoskeletal protein essential for the maintenance of spine morphology in contrast to the signal molecule MARCKS, and reduction of SPTA2 by itself is harmful to dendritic spine formation. In any case, these results further supported that the MARCKS and SPTA2 are the critical target molecules of overactivated PKC and CamKII kinases, and that abnormal phosphorylation of these proteins functionally impairs synaptic spines in the early stage of the AD pathology. In western blot, we confirmed suppression of MARCKS

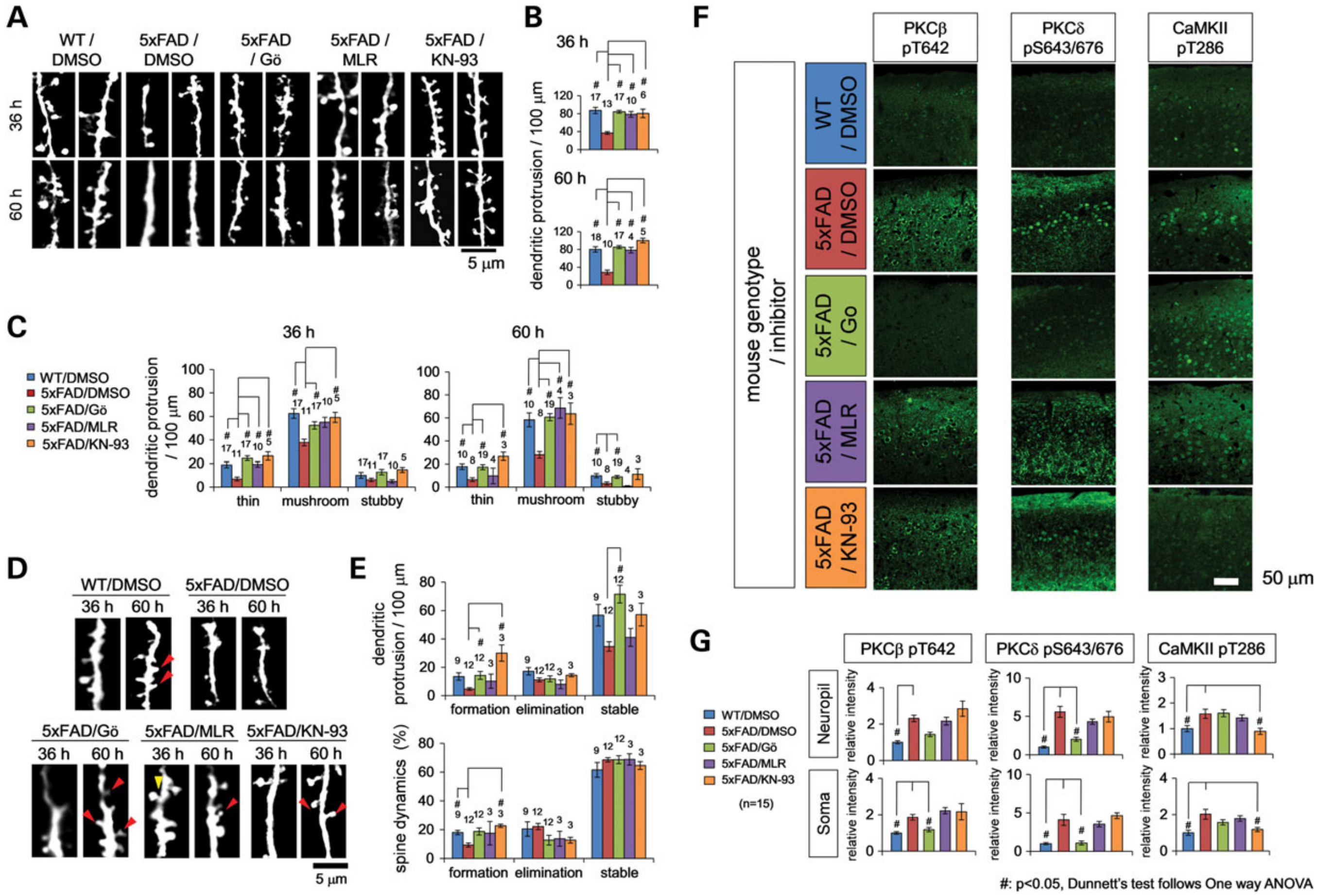

Figure 4. Modulation of MARCKS kinases recovers spine pathology at early AD stage. (**A**) Representative images of dendritic spines/protrusions in layer 1 of the retrosplenial cortex of background B6/SJL (WT), 5xFAD and drug-treated (Gö6976, MLR1023 and KN-93) 5xFAD mice at 12 weeks observed by two-photon microscopy *in vivo*. 5xFAD mice exhibited a definitely lower number of protrusions, whereas Gö6976 (PKC inhibitor), MLR1023 (Lyn activator) and KN-93 (CamKII inhibitor) treatment led to a recovery of the decrease in spines in 5xFAD mice. (**B**) Quantitative analysis of dendritic spine densities in four types of mice at 36 or 60 h after drug treatment. Mock treatment with DMSO was also performed. Mean ± SEM are shown. Statistical analyses were performed by two methods. $^{**}P < 0.01$ in Student's unpaired *t*-test. $\#P < 0.05$ in one-way ANOVA *post hoc* Dunnett's test. Sample numbers are shown in the figure. We used three mice for each group and obtained data with 1–4 dendritic neurites from a mouse. The numbers of neurites used for the analyses are indicated above the bar. (**C**) Quantitative analysis of spine types at 36 or 60 h after drug treatment. Regardless of morphological type, spine density was decreased in 5xFAD mice, and the decrease was recovered by Gö6976, MLR1023 and KN-93 treatment. Mean ± SEM are shown. $^{*}P < 0.05$, $^{**}P < 0.01$ in Student's unpaired *t*-test. #: $P < 0.05$ in one-way ANOVA *post hoc* Dunnett's test. Sample numbers are shown in the figure. (**D**) Representative images of spine formation and elimination observed in each type of mice from 36 to 60 h. The red arrow indicates spine formation and the yellow arrow indicates spine elimination. (**E**) Quantitative analysis of dendritic spine dynamics. The upper panel shows the number of spines that were formed, eliminated or remained stable in 100 µm of a dendritic shaft during observation. The lower panel shows the relative percentage of the formation, elimination and stability of spines. In 5xFAD mice, spine formation and stability per length were decreased, whereas their elimination was not significantly changed (upper panel). The ratios of the three types of spine dynamics were not different among the four types of mice (lower panel), indicating that the efficiency of spine formation was simply decreased. The decrease in the number of stable spines per length reflected the reduced number of spines per length. Mean ± SEM are shown. $^{*}P < 0.05$, $^{**}P < 0.01$ in Student's unpaired *t*-test. $\#P < 0.05$ in one-way ANOVA *post hoc* Dunnett's test. Sample numbers are shown in the figure. (**F**) Immunohistochemistry of cerebral cortex of wild-type (background B6/SJL, DMSO treated), 5xFAD (DMSO treated), 5xFAD (Gö6976 treated), 5xFAD (MLR1023 treated) and 5xFAD (KN-93 treated) mice with antibodies against activated PKCβ, PKCδ and CamKII. Specific inhibition by each inhibitor was confirmed. (**G**) Quantitative analysis of the signals of each activated kinase in neuronal soma or neuropil. We used three mice for each group and obtained data with five visual fields from a single mouse ($n = 15$).

and SPTA2 proteins by their shRNA-lentiviral vectors in the brain tissues adjacent to the observation area with two-photon microscopy (Supplementary Material, Fig. S12).

We also tested the validity of the second functional focus of the core proteins, synaptic vesicle recycling in which SYT1/synaptotagmin1 and CLH/clathrin heavy chain were involved. SYT1 is a transmembrane protein possessing two C2 domain. In the linker portion between the transmembrane domain and C2 domains, three phosphorylation sites of CamKII, PKC and CaskII were reported. CLH forms triskelion and coats synaptic vesicle. Modulation of phosphorylation site of SYT1 detected in this study actually influenced recycling of synaptic vesicle in primary culture, which will be reported elsewhere (data not shown).

Subnetwork changes in AD pathology

Finally, we performed a subnetwork analysis using our phosphoproteome data to reevaluate various signaling pathways that had been implicated in AD pathology. We used the pathway maps of

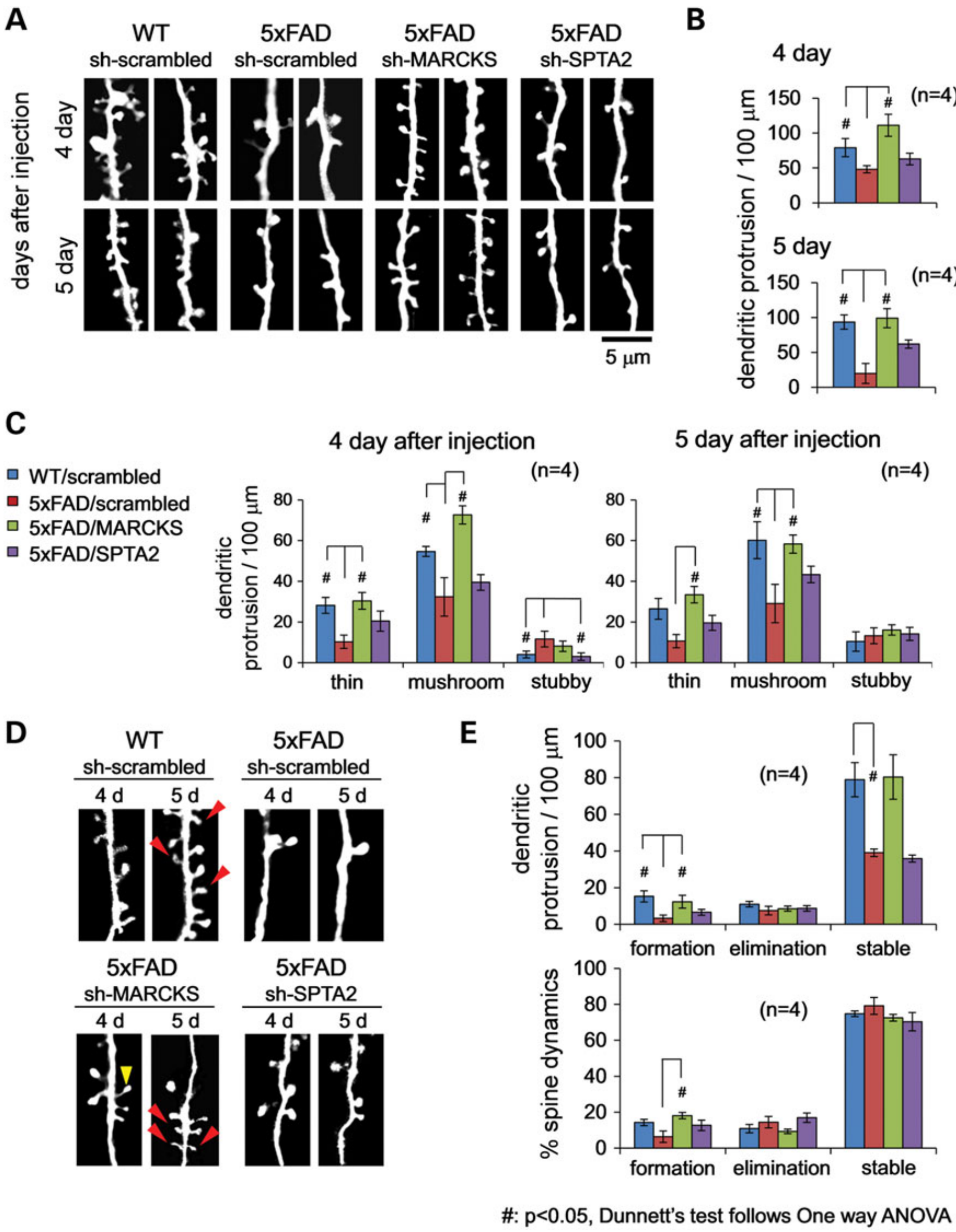

Figure 5. MARCKS knockdown recovers spine pathology at early AD stage. (**A**) Representative images of dendritic spines/protrusions in layer 1 of the retrosplenial cortex of sh-RNA-lentiviral vector-injected background B6/SJL (WT) or 5xFAD mice observed by two-photon microscopy *in vivo*. Lentiviral vector (Sh-RNA-MARCKS, Sh-RNA-SPTA2 or scrambled shRNA) was injected and images were obtained 4 and 5 days after injection by two-photon microscopy as described in Materials and Methods. Decrease of dendritic spines in 5xFAD mice was recovered by Sh-RNA-MARCKS but not Sh-RNA-SPTA2. (**B**) Quantitative analysis of dendritic spine densities at 4 or 5 days after injection. Mean ± SEM are shown. Statistical analyses were performed by two methods. $^{*}P < 0.05$, $^{**}P < 0.01$ in Student's unpaired *t*-test. #: $P < 0.05$ in one-way ANOVA *post hoc* Dunnett's test. Sample numbers are shown in the figure. We used four mice for each group and obtained data with 1–4 dendritic neurites from a mouse. (**C**) Quantitative analysis of spine types at 4 or 5 days after injection. Sh-RNA-MARCKS recovered the decreased thin protrusions in 5xFAD mice at 4 and 5 days after injection. Mushroom-type protrusions were recovered at 5 days. Sh-RNA-SPTA2 did not recover those protrusions sufficiently. Mean ± SEM are shown. $^{*}P < 0.05$, $^{**}P < 0.01$ in Student's unpaired *t*-test. #: $P < 0.05$ in one-way ANOVA *post hoc* Dunnett's test. Sample numbers are shown in the figure. (**D**) Representative images of spine formation and elimination observed in each type of mice from 4 to 5 days. The red arrow indicates spine formation and the yellow arrow indicates spine elimination. (**E**) Quantitative analysis of dendritic spine dynamics. The upper panel shows the number of spines that were formed, eliminated or remained stable in 100 μm of a dendritic shaft during observation. The lower panel shows the relative percentage of the formation, elimination and stability of spines. Mean ± SEM are shown. $^{*}P < 0.05$ in Student's unpaired *t*-test. #$P < 0.05$ in one-way ANOVA *post hoc* Dunnett's test. Sample numbers are shown in the figure.

KEGG (http://www.kegg.jp/kegg/), NCBI Biosystems (http://www.ncbi.nlm.nih.gov/biosystems/) and AmiGO (http://amigo.geneontology.org/cgi-bin/amigo/go.cgi) and tested whether phosphoproteins from a specific signaling pathway were changed in the four types of AD mouse models at statistically high odds. We used different mother populations (total phosphoproteins changed in proteomics analysis or total proteins registered in Uniprot) to test whether phosphoproteins belonging to a specific signaling network were changed significantly rather than stochastically (Supplementary Material, Table S7).

The results of these analyses indicated that the TNF, MAP kinase and Wnt signaling pathways were significantly changed in the early stage of AD pathology (Supplementary Material, Table S7). In addition, these results suggested that insulin, Fyn, ER damage, mitochondrial stress, oxidative stress, GPCR, inflammation, cAMP/Ca^{2+}, autophagy and PI3 kinase signaling pathways might also be affected (Supplementary Material, Table S7). The subnetworks identified (Supplementary Material, Fig. S13) and the proteins included in them are shown in Supplementary Material, Table S8. Extensive computational analyses of the subnetwork database would be useful to predict candidate molecules and/or specific signaling pathways that could be used to develop candidate drugs to treat AD. Alternatively, they would help to prevent exposure environmental factors that accelerate AD. For instance, the b-raf (which is involved in insulin signaling), autophagy-mTOR signaling and TNF signaling pathways (Supplementary Material, Table S7) may be interesting targets for therapeutic development.

We performed similar functional subnetwork analysis with human AD brains. Subnetworks were generated based on phosphoproteins changed in temporal/occipital lobe tissues from human AD patients, and compared with the networks generated with cortex tissues from 5xFAD mice at 1–6 months. Signaling pathways changed commonly in 5xFAD mice and human AD patients included Fyn, Toll-like receptor 4 and PI3K-AKT pathways (Supplementary Material, Fig. S14).

Candidate proteins involved in transition from amyloid to tau pathology

In addition to identification of the early stage AD-specific network, we also intended to identify new kinases that could promote tau phosphorylation. AD core phosphoproteins based on hypothesis-free approach did not directly include any kinase/phosphatase at $P < 0.05$ (Supplementary Material, Table S2). However, at $P < 0.05$, b-raf was found in two AD models at 3 months, and at $P < 0.10$, it was found in three AD models at 1 month and two AD models at 6 months (Supplementary Material, Table S2). Moreover, subnetwork analysis suggested the importance of b-raf in multiple signal networks including insulin, autophagy, MAP kinase and TNF signaling pathways. Therefore, we suspected that b-raf might be located at the link of multiple signaling pathways and could be a continuous enhancer of the transition from amyloid to tau pathologies in AD mice.

Hence, we tested whether the inhibition of b-raf actually modulated tau pathology. We added Aβ and three types of b-raf inhibitors to primary cultures of cortical neurons. As expected, phosphorylation of tau was suppressed in Aβ-treated cortical neurons (Supplementary Material, Fig. S15A and B), which was consistent with the idea that b-raf may be a molecule that promotes the transition from amyloid pathology to tau pathology. This finding also indicates that GPCR ligands that are relevant to b-raf might accelerate the AD signaling pathway.

As described in a previous section, an increased phosphorylation of tau was shared by severe AD (5xFAD, APP) and tau model mice at 1 month (Supplementary Material, Table S2). Surprisingly, tau phosphorylation started in the brain of young AD mice (1 month) far before immunohistochemical (Supplementary Material, Fig. S3) and symptomatic change (Supplementary Material, Fig. S4). Therefore, it is possible that b-raf is involved in the transition from amyloid to tau pathology. However, tau phosphorylation did not sustain in the AD mice after 3 months (Supplementary Material, Table S2) and did not reach to the histological level of tau mice (Supplementary Material, Fig. S3), suggesting that additional factors are necessary to develop to tau pathology.

DISCUSSION

In this study, we first performed a comprehensive phosphoproteomics analysis using brain samples from multiple mouse models and patients with AD, which allowed us to identify whole aspects of the phosphoproteomics changes that occur in disease-stage- and region-specific manners. Our approach using systems biology also extracted a limited number of core molecules, the phosphorylation states of which played central roles at the early stage (non-symptomatic stage) of AD pathology. Importantly, two algorithms selected basically similar proteins as the target of abnormal phosphorylation. Surprisingly, most of these core molecules were physically and functionally connected, and composed a single PPI network that covers synapse formation, synaptic vesicle recycling and energy production that supports the first two functions (Fig. 2; Supplementary Material, Fig. S8). Especially, systems biology analyses expected that MARCKS was most critical in the early stage of AD pathology because chronological changes of MARCKS in four AD models were analogous to those of multiple core proteins (Supplementary Material, Fig. S9C) that were directly linked to MARCKS in PPI databases (Supplementary Material, Fig. S7) and sequentially activated during the progression of pathology in 5xFAD mice (Supplementary Material, Fig. S9E).

Consistently, we confirmed that MARCKS and kinases that target MARCKS such as PKC and CamKII contributed to the spine pathology by *in vivo* experiments using shRNA or kinase inhibitors (Figs. 4 and 5). Interestingly, abnormal phosphorylation of the core proteins was changed dynamically during the progression of AD pathology. MARCKS and some relevant phosphoproteins were changed most significantly at the early stage (Supplementary Material, Fig. S9D and E), while abnormal phosphorylation of the other proteins occurred from the middle to the late stage in the brain of model mouse brain (Supplementary Material, Fig. S9D and E; Fig. 3).

In vivo imaging with two-photon microscopy revealed that MARCKS plays a critical role in abnormal morphology and dynamics of synaptic spines that have been implicated in the AD pathology. Given that presynaptic BASP1 (30) and NEUM/GAP43 (46,47) showed a similar pattern of abnormal phosphorylation, it is possible that not only post-synapse but also presynapse are functionally impaired from the middle stage of AD pathology. Though not reported in this study in detail, impaired synaptic vesicle recycling through abnormal phosphorylation of SYT1 and CLH might be a critical domain of presynaptic pathology.

This study casted a light again on the role of PKC in AD, since more than a half of the core molecules are targets of PKC (Supplementary Material, Table S6). Obviously, PKC contributes to memory formation (48,49). Calcium influx from the NMDA receptor enhances CREB-dependent transcription of BDNF and Arc via the activation of PKC and CaMKII (50). Based on such transcriptional activation, PKC has been considered to be protective against AD (51). Conversely, the opposite role of PKC on the stability of synapses has been described under physiological (non-AD) condition (22), and overactivation of PKC seems to be harmful for working memory (52).

In this controversy, our nonbiased comprehensive proteomics study indicated that PKC is harmful for synaptic spine formation (Figs. 4 and 5) especially at the early stage of AD pathology before histological Aβ aggregation (Supplementary Material, Fig. S3). This conclusion might be different from the common sense but is actually consistent with the hyperactive synapse hypothesis at the early AD stage (16). Concomitantly, the subsequent decline in the phosphorylation of these PKC targets observed in mice aged 3–6 months and in autopsied human brains (Supplementary Material, Fig. S7) supports the concept that a hypoactive synapse state occurs with the progress of Aβ deposition (Supplementary Material, Fig. S3).

Pathological roles of PKC in synaptic impairment of AD remain unclear. Two groups demonstrated independently the immunoreactivity of PKC in the periphery of senile plaques, where degenerative dendrites or axons are concentrated (53,54). In contrast, the therapeutic effects of a PKC activator have also been reported, in which bryostatin 1 dramatically enhances the secretion of the α-secretase product sAPPα in fibroblasts from patients with AD and reduces Aβ40 levels in the brains of APP transgenic mice (55). However, its relevance has been limited to Aβ production, and the direct pathological role of PKC in synapse deterioration is unknown. In this regard, our findings could be a hint to solve the old question.

The second kinase shown to be involved in the early AD stage was CamKII. CamKII beta is known to bundle actin (56) and transient activation of CamKII within 1 min is associated for spine enlargement linked to LTP (57). Overexpression of non-phosphorylated form of CamKII induced enlargement of spines (58) while phosphorylation of CamKII lead to uncoupling of actin (56). Therefore, phasic phosphorylation of CamKII is essential for spine formation, but tonic phosphorylation of CamKII might impair actin recycling and inhibit spine growth. Given that inhibitor of CamKII ameliorated the spine morphology, this study revealed that such tonic activation contributed to worsen the synapse pathology at the early stage of AD (Fig. 4A–G).

In addition to PKC and CamKII that had been implicated in AD in previous research, this study identified several new kinases, the significance of which had been insufficiently recognized. Lyn kinase was a particular example; this protein regulates an energy metabolism-related protein G3P/GAPDH, which was identified to link to various molecules in the AD core network (Fig. 1C) and involved in the insulin–mimetic signaling pathway via the insulin-receptor substrate protein 1 (58).

In this study, we did not focus on SRRM2/SRm300, although it was hyperphosphorylated in the early-middle stage of model mice (Supplementary Material, Fig. S9D and E). SRRM2/SRm300, serine/arginine repetitive matrix 2, was a component of catalytic spliceosome and was a very interesting target of phosphorylation signal. In addition, it was suggested as a remarkably changed gene in substantia nigra of the Parkinson's disease (59). Interestingly, the shorter transcript of SRRM2/SRm300 was increased while the longer transcript was decreased. The result indicated that splicing of SRRM2/SRm300 by itself was changed. Although RNA splicing was implicated in various neurodegenerative diseases like TDP43-associated FTLD, pathological contribution of this molecule to AD pathology remains unclear at this moment.

Finally, it would be of worth to add some minor findings in this study. The phosphoproteins changed specifically in human AD brains included interesting molecules (Supplementary Material, Fig. S6b). In particular, the protein phosphatase 1 regulatory subunit 14A (PP14A) and osteopontin (OSTP), which were detected in the intersection of the temporal and occipital lobe groups (Supplementary Material, Fig. S6a) were specific to AD and not detected in DLB (Supplementary Material, Fig. S6a). PP14A has not been directly implicated in AD. However, PP1 is a suppressor of learning and memory, and the inhibitory effect of PP14A on PP1 was dramatically enhanced by PKC-dependent phosphorylation (60). Moreover, its phosphorylation was changed in neurotrauma (61) and a connection with JNK was reported in the signaling induced by hydrogen peroxide (62). Phosphorylation of PP14A was increased consistently in our analysis. In contrast, the increase (63) or decrease (64) in OSTP in the cerebrospinal fluid of patients with AD was directly implicated. Phosphorylation regulates the biological function of OSTP (65,66) which is a protein that may affect mTOR signaling (67).

From the viewpoint of biomarker, it is of note that SYT1 and NEUM are largely changed in aggregation-positive models (5xFAD and APP) but not in aggregation-negative models (PS1 and PS2). The two proteins showed middle stage pattern of chronological changes, inspiring the hypothesis that their phosphorylation is induced by accumulation of Aβ preaggregates developing to senile plaque. SYT1 and NEUM might be more sensitive than the other core network proteins in phosphorylation response to Aβ preaggregation in the early stage. The other candidate could be MARCKS, ADDB and SPTA2 that were changed in human AD brains. Combinatory use of multiple phosphoproteins that changed at different stages might be more sensitive and prognostic. Interestingly, subnetwork analysis indicated increased phosphorylation of stathmin, which was recently reported to be available as a biomarker in CSF of human AD patients (68), in TNF and MAP kinase signaling pathways (Supplementary Material, Fig. S13).

We strictly excluded human AD brains in which other types of pathological changes (Lewy bodies, TDP43 cytoplasmic aggregates or argyrophilic grains) were contaminated. The criterium was essential to exclude phosphoproteomic changes related to the other types of pathology. Furthermore, we used DLB as a disease control. It is of note that from the human data MARCKS was again proven as an AD-specific (DLB-non-included) phosphoprotein (Supplementary Material, Fig. S6b). On the other hand, this strict approach decreased the number of usable samples of human AD patients in this study. A future study using >100 brains with a low level of pathological restriction for samples might be interesting in comparison to our very strict results.

Finally, it was unexpected that molecular changes at the early stage of model mice were still observed in postmortem human AD brains at the terminal stage. The reason is not clear while we can speculate that AD molecular pathology newly initiates in a part of brain regions and a group of neurons of human AD brains even at the terminal stage. This hypothesis would explain why phosphorylation of MARCKS and other AD core proteins were still changed at the terminal phase of human AD pathology.

In conclusion, this study provided us useful information for reevaluation and progression of understanding of AD.

MATERIALS AND METHODS

Mouse brains

PS1 transgenic mice expressing the exon 9 deletion mutant (PSEN1dE9) under the control of the mouse *PrP* promoter (69); PS2 transgenic mice expressing human mutant PS2 (N141I) under the control of a ubiquitous CMV early enhancer and the chicken β-actin promoter (70); mice transgenic for the human double-mutant APP_{770} (KM670/671NL; Swedish type) inserted into a hamster PrP cosmid vector by replacing the *PrP* gene with the mutant APP (71); 5xFAD transgenic mice expressing the mutant human APP_{770} with Swedish (KM670/671NL), Florida (I716V) and London (V717I) triple mutations, as well as human PS1 harboring double mutations (M146L and L285V) under the mouse *Thy1* promoter (72); and transgenic mice for the human mutant Tau protein under the control of the mouse *PrP* promoter (73) were used. Their backgrounds were C57BL/6J, C57BL/6J, C57/B6XSJL/F1, C57/B6XSJL/F1 and C57/B6XC3H/F1, respectively. Mass analysis was performed with brain tissues from male mice at the age indicated in the figure or legend.

For immunohistochemistry, brain samples were fixed in 4% paraformaldehyde, and paraffin sections (5 µm each) were obtained using a microtome (Yamato Kohki Industrial Co., Ltd., Saitama, Japan). Immunohistochemistry was performed using primary antibodies (anti-Aβ, 82E1, IBL, Gunma, Japan, Cat # 10323; anti-Aβ, 6E10, Covance, NJ, USA, Cat # SIG-39300; and anti-human PHF-tau, AT-8, Innogenetics, Ghent, Belgium, Cat # BR-03; dilution, 1:1000 each) and reaction products were visualized with the Vectastain Elite ABC kit and DAB Peroxidase Substrate kit (Vector, CA, USA).

For behavioral tests, male mice at the indicated age in the figure or legend were used. Six types of behavioral tests were performed for individual mice of all AD and tau models. In the Morris water maze test, mice received four trials (60 s) per day for 5 days, and the latency to reach the platform was measured. In the rotarod test, mice received four trials (3.5–35 rpm) per day for 3 days, and the mean latency to fall off the rotarod was recorded. In the fear-conditioning test, the rate of the freezing response of mice was measured in the same conditioning chamber (65 dB white noise, 30 s) in the absence of the foot shock (0.4 mA, 2 s) at 24 h after the conditioning trial. The duration of the stay at the central area of an open-field space was adopted as the index of the open-field test. In the light–dark box test, the duration of the stay in the light box was measured. The elevated plus maze was set up 60 cm above the floor, and the duration of the stay in the open arms was measured.

Human brains

Brain samples for proteome analysis were dissected from AD, DLB and normal control bodies and deep frozen (−80°C) within 1 h after death. A neuropathologist (S.M.) established the pathological diagnosis of the brains based on immunohistochemistry. AD brains did not include other pathological changes, such as Lewy bodies, TDP43 cytoplasmic aggregates or argyrophilic grains. DLB brains also showed specific pathological findings. Temporal pole and occipital pole tissues were dissected from five brains from each group. Control brains were derived from age-matched patients who died due to non-neurological diseases.

Preparation of phosphorylated proteins and peptides

Cerebral cortices were collected from mice within 5 min after their sacrifice by deep euthanasia with ethyl ether. Cerebral cortices were frozen in liquid nitrogen immediately and kept until use. The cortical tissue was lysed in cold lysis buffer containing 2% SDS, 1 mM DTT, and 100 mM Tris–HCl (pH 7.5) and homogenized using 20 strokes of a Dounce glass homogenizer on ice. The ratio of lysis buffer to tissue was 10 volumes (µL) to 1 weight (mg). Subsequently, the lysate was incubated at 100°C for 15 min. The crude extract was centrifuged at 16 000*g* at 4°C for 10 min. The supernatant was diluted to a 1/10 concentration with water and filtered through a 0.22 µm filter. The flow-through was concentrated to 10-fold using an Amicon Ultra 3K filter (Millipore, MA, USA). The concentration of proteins was measured using the BCA Protein Assay Reagent (Thermo Fisher Scientific, Inc., MA, USA). Sample aliquots (200 µL) containing 1.5 mg of protein were added to 100 µL of 1 M triethylammonium bicarbonate (TEAB) (pH 8.5), 3 µL of 10% SDS and 30 µL of 50 mM tris-2-carboxyethyl phosphine, followed by incubation for 1 h at 60°C. Cysteine residues were blocked with 10 mM methyl methanethiosulfonate for 10 min at 25°C. Then, samples were digested with trypsin (mass analysis grade) (10 : 1 protein/enzyme, w/w) in 80 mM $CaCl_2$ for 24 h at 37°C.

Phosphopeptides were enriched using the Titansphere Phos-Tio Kit (GL Sciences Inc., Tokyo, Japan), and desalted using a Sep-Pak Light C18 cartridge column (Waters Corporation, MA, USA), according to the manufacturer's instructions. The sample aliquots were dried and dissolved with 25 µL of 100 mM TEAB (pH 8.5). The phosphopeptides in each individual sample were labeled separately using the iTRAQ Reagent multiplex assay kit (AB SCIEX Ins., CA, USA) for 2 h at 25°C, according to the manufacturer's instructions. The labeled phosphopeptide pools were then mixed together. The aliquots obtained were dried and then redissolved in 1 ml of 0.1% formic acid.

2D LC–MS/MS analysis

The labeled phosphopeptide samples were subjected to strong cation exchange chromatography using a TSK gel SP-5PW column (TOSOH, Tokyo, Japan) on a Prominence UFLC system (Shimadzu, Kyoto, Japan). The flow rate was 1.0 ml/min with solution A (10 mM KH_2PO_4, pH 3.0, 25% acetonitrile). Elution was performed with solution B (10 mM KH_2PO_4, pH 3.0, 25% acetonitrile, 1 M KCl) in a gradient ranging from 0 to 50%. The elution fractions were dried and dissolved in 100 µL of 0.1% formic acid.

Each fraction was analyzed using a DiNa Nano-Flow LC system (KYA Technologies Corporation, Tokyo, Japan) at the flow rate was 300 nL/min. For the NanoLC, samples were loaded onto a 0.1 × 100 mm C18 column with solution C (2%

acetonitrile and 0.1% formic acid) and eluted with a gradient of 0–50% solution D (80% acetonitrile and 0.1% formic acid). The ion spray voltage to apply sample from NanoLC to Triple TOF 5600 System (AB SCIEX Ins., CA, USA) was set at 2.3 kV. The information-dependent acquisition (IDA) setting was 400–1250 *m/z* with two to five charges. The Analyst TF1.5 software (AB SCIEX Ins., CA, USA) was used to identify each peptide. The quantification of each peptide was based on the TOF-MS electric current detected during the LC-separated peptide peak, adjusted to the charge/peptide ratio. The signals were analyzed by Analyst TF (version 1.5) (AB SCIEX Ins., CA, USA) and processed by ProteinPilot software (version 4) as described in the following.

Data analysis

Acquisition and analysis of mass spectrum data of peptides were performed by Analyst TF (version 1.5) (AB SCIEX Ins., CA, USA). Using the results, we searched corresponding proteins from database of mouse and human protein sequences (UniProtKB/Swiss-Prot, downloaded from http://www.uniprot.org on June 22, 2010) by ProteinPilot (version 4) (AB SCIEX Ins., CA, USA) that employs Paragon algorithm (74). Tolerance for the search of peptides by ProteinPilot was set to 0.05 Da for the MS and 0.10 Da for the MS/MS analyses, respectively. 'Phosphorylation emphasis' was set at sample description, and 'biological modifications' was set at processing specification of ProteinPilot. The confidence score was used to evaluate the quality of identified peptides, and identified proteins were grouped by the ProGroup algorithm (AB SCIEX Ins., CA, USA) to exclude redundancy. The threshold for protein detection was set at 95% confidence in ProteinPilot, and proteins with >95% confidence were accepted as identified proteins.

False discovery rate (FDR) was calculated using Target-decoy search strategy (75). All protein sequences in fasta were downloaded from UniProtKB/Swiss-Prot (http://www.uniprot.org/downloads) as target and their reverse sequences were generated as decoy. With peptide sequences identified in our mass analysis, we searched the target and decoy databases and calculated false positive (FP = 2 × passing decoy assignments) and true positive (TP = total passing assignment − number of FP). FDR was calculated by FP/(TP + FP). FDR values corresponding to proteins and peptides (confidence > 95%) are shown in Supplementary Material, Table S1.

Quantification of proteins was performed through analysis of iTRAQ reporter groups in MS/MS spectrum that are generated upon fragmentation in the mass spectrometer. In quantification of peptides and proteins, bias correction that assumes the total signal amount of each iTRAQ should be equal was employed to normalize signals different iTRAQ reporters. In quantification of peptides and proteins, bias correction option was used to normalize different iTRAQ signals.

Peptide ratio, the ratio between reporter signals in AD models and that of control samples, was calculated also after bias correction. Then protein ratio (average ratio) was deduced by weighted average of peptide ratios corresponding to the protein, where peptide ratios were differentially weighted based on error factors, after bias correction. The detailed formulas to calculate these values were described in the manual from ABSCIEX. In brief, after excluding peptides without iTRAQ label, those sharing MS/MS, and those having a low intensity, log values of iTRAQ ratios corresponding to a peptide were summed. Ten to the power of the sum value was divided by bias. The result was treated as quantity of the peptide.

Protein quantities in AD sample were compared with that in control sample using the peptide ratio. Student's *t*-value was calculated from weighted average of log peptide ratio, its standard error, and log bias. Then the *P*-value was calculated together with a *post hoc* test in ProteinPilot (not disclosed in detail) to exclude multiple hypothesis testing issues. The *P*-values of three samples provided from this test were integrated by inverse normal method. Phosphoproteins were judged changed, when the integrated *P*-value was <0.05 (Supplementary Material, Table S2).

The results in peptide summary and protein summary of ProteinPilot were imported to Excel files for further data analyses. Quantity of a phophopeptide fragment was calculated as the geometric mean of signal intensities of multiple MS/MS fragments including the phosphorylation site. Difference between AD group and control group was tested by student's *t*-test ($n = 6$) (Supplementary Material, Table S5). We compared changed phosphoproteins among different AD models and selected the commonly changed proteins in hypothesis-free- or Aβ aggregation-linked approach (Supplementary Material, Table S2).

Systems biology

We used the software Protein Pilot version 4 (AB SCIEX, CA, USA) to identify proteins expressed in human brain occipital and temporal lobes. Protein Pilot also added Uniprot ID to each observed protein, automatically. We then searched for proteins that shared the common Homologene Group ID of each observed protein and obtained the Taxonomy IDs and Gene IDs of the collected proteins. We noted that the Taxonomy ID was restricted to 9606 (human), 10090 (mouse) or 10116 (rat). Uniprot IDs of newly added proteins were also attached. From the list of collected proteins, we removed proteins whose Uniprot IDs were not listed in the GNP database (http://genomenetwork.nig.ac.jp/index_e.html); we created a database of GNP-collected information on the Supercomputer System available at the Human Genome Center of the University of Tokyo. We called the remaining proteins analyzed proteins. We searched for proteins that interacted with the analyzed proteins in the GNP database and created the edge file (redundant edges were removed). The protein network was obtained based on the created edge file and visualized using Cell Illustrator (76).

Subnetwork analysis

Among the protein functional categories available in KEGG (http://www.kegg.jp/kegg/), NCBI BioSystems (http://www.ncbi.nlm.nih.gov/biosystems/) and AmiGO (http://amigo.geneontology.org/cgi-bin/amigo/go.cgi), we selected 23 groups of signaling pathways that have been reported to be relevant to AD. To determine the 23 categories, we searched three databases with AD-pathology-related genes or functional terms (insulin, fyn, hippo, etc.) that had been implicated in AD by previous research; we used pathways that included the term in the pathway name. In addition, we screened pathway-linked information, including component proteins and related functions of three databases

(KEGG, NCBI BioSystems and AmiGO), and used the pathway if the term was included in linked information. We calculated the probability of the number of mass-identified phosphoproteins being included and of the remaining proteins not being included in the selected pathways with reference to the total number of identified proteins (1477 proteins) or the total number of mouse proteins in the Uniprot database (74812 proteins) using the hypergeometric distribution method; we also determined the *P*-value. We used Cell Illustrator to draw the subnetworks identified in AD pathology.

In vivo imaging via two-photon microscopy

Two-photon imaging of dendritic spines was performed using a laser-scanning microscope system FV1000MPE2 (Olympus, Tokyo, Japan) equipped with an upright microscope (BX61WI, Olympus, Tokyo, Japan), a water-immersion objective lens (XL PlanN25xW; numerical aperture, 1.05) and a pulsed laser (MaiTaiHP DeepSee, Spectra Physics, CA, USA). EGFP was excited at 890 nm and scanned at 500–550 nm. The scanning area used for three-dimensional imaging was 100×100 μm (1 μm *Z*-steps, 1024×1024 pixels). Two weeks before imaging, adeno-associated virus 1 (AAV1)-EGFP with the synapsin I promoter (titer 1×10^{10} vector genomes/mL, 1 μL) was injected into the retrosplenial cortex (anteroposterior, −2.0 mm and mediolateral, 0.6 mm from bregma; depth, 1 mm) of mice under anesthesia with 2.5% isoflurane. The dendritic spines of the mouse cortical layer 1 were imaged through a thinned-skull window, as described previously (77). Alzet micro-osmotic pumps (model 1003D, Durect Corporation, CA, USA) filled with PBS/0.1% DMSO containing 1 μM Go6976 (78) (Calbiochem, CA, USA), 1 μM MLR1023 (79) (Glixx Laboratories, MA, USA) or 0.4 mM KN-93 (80) (Cayman, MI, USA) were implanted into the O_2/isoflurane-anesthetized mice. Dendritic spines were observed 36 and 60 h after implantation. For injection of shRNA-lentiviral vectors, 3 μl of lentiviral vector for Sh-RNA MARCKS (sc-35858-V, Santa Cruz, TX, USA; 1×10^6 TU), Sh-RNA SPTA2 (mixture ofV3LMM_423737, V2LMM_104859 and V2LMM_202472, Thermo, MA, USA; 1×10^8 TU) or scrambled shRNA (RHS4348, Thermo Scientific, MA, USA; 1×10^6 TU) was injected to same region as the AAV1-EGFP. Images were analyzed for spine density, spine length, spine maximum diameter and spine neck minimum diameter using IMARIS 7.2.2 (Bitplane, Zurich, Switzerland).

Treatment of primary culture cortical neurons with b-raf inhibitors

Mouse cerebral cortexes from 15-day-old embryos of C57BL/6J were dissected and minced into fine pieces and rinsed with PBS. After incubation with 0.05% trypsin for 10–15 min at 37°C following treatment with 25 μg/ml of DNase for 5 min at 37°C, the dissociated cells were washed twice with DMEM (Sigma–Aldrich, MI, USA) containing 50% FBS. Cells were centrifuged at 100*g* for 1 min, resuspended in 10% FBS/DMEM, gently triturated with blue tips and filtered through a nylon mesh (Falcon 2350; BD, NJ, USA) to remove any debris. The isolated cells were centrifuged at 100*g* again for 5 min and were collected. Cells were resuspended in Neurobasal medium (Life Technologies, CA, USA) with B-27 supplement (Life Technologies, CA, USA) and plated 1.7×10^6 cells/well in the six-well plastic plate (Corning, NY, USA) coated with poly-L-lysin (Sigma–Aldrich, MI, USA) in 0.15 M borate buffer (pH 8.4). Cells were incubated in 5% CO_2 at 37°C. To remove proliferating glial cells, arabinosylcytosine (Sigma–Aldrich, MI, USA) was added to the culture medium (4 μM) on the next day. After 7 days, b-raf inhibitors, PLX4720 (Selleck Chemicals, TX, USA, 1 or 10 μM), Sorafenib (Selleck Chemicals, TX, USA, 1 or 10 μM) and GDC-0879 (Selleck Chemicals, TX, USA, 1 or 10 μM) were added to the medium at first, and after 3 h 10 μM Aβ 1–42 peptide (Peptide Institute, Inc., Tokyo, Japan) was added to the medium. The neurons were collected after another 3 h.

MS/MS with SWATH acquisition

Phosphopeptide samples were similarly prepared from 5xFAD and background mice to the step of enrichment by the Titansphere Phos-Tio Kit (GL Sciences Inc., Tokyo, Japan). After desalting by a Sep-Pak Light C18 cartridge column (Waters Corporation, MA, USA), the samples were dried and dissolved in 30 μL of 0.1% formic acid. 10 μL aliquot was applied to 0.1×100 mm C18 column (KYA Technologies Corporation, Tokyo, Japan) with solution E (0.1% formic acid) and eluted with a gradient of 2–40% solution F (99.9% acetonitrile and 0.1% formic acid) using 300 nL/min of flow rate in Eksigent NanoLC-Ultra 1D plus system (AB SCIEX Ins., CA, USA), and subjected to Triple TOF 5600 system at 2.3 kV of ion spray voltage. The IDA was set at 400–1000 *m/z* with two to five charges, and the product ion MS/MS scan range was between 100 and 1600 Da with an accumulation time of 100 ms for spectral library. SWATH acquisition was performed by 24 sequential windows of 25 Da that spanned from 400 to 1000 Da (81). SWATH acquisition of the MS/MS spectral data was performed by the Analyst TF1.5 software (ABSciex Ins., CA, USA) for 100 ms/window and the MS/MS spectral library was prepared by the Protein Pilot software (version 4.5). Peakview software (version 1.2.0.3) correlated the MS/MS spectral data with peptide data and LC retention time. The MS/MS product ions from the same peptide were summed and used as quantity of the peptide.

Statistics

Mass spectrometry data of disease model mice or human patients were evaluated by normal inversion method with the data of their background mice or human control samples, respectively. Given that the amount of each peptide was supported multiple peaks in mass spectrometry and that the amount of each protein was supported by multiple peptide values, their quantities possessed *P*-value. Together with the *P*-values, differential expression analysis with each peptide or protein can be performed without replication. To guarantee the quality of the results, we furthermore took biologically replicated data that can increase the number of identified proteins as well. Therefore, the sample size of human or mouse brains ($N = 5$ and 3, respectively) was considered appropriate. We did not check whether all samples form normal distribution. However, in the process of computing *P*-values, the commercial program used in this study (Protein Pilot) removed low-quality measurement that causes outliers. The results from animal behavior tests and two-photon microscopy were analyzed basically by Student's unpaired *t*-test (two sided) with the sample size described in the legend for each figure. Sampling of brain tissues, mass data acquisition and systems biology analyses were performed by independent investigators without knowing group allocation.

Ethics

This study was performed in strict accordance with the recommendations in the Guides for the Human Genome and Gene Researches of Ministry of Health, Labour and Welfare and the Care and Use of Laboratory Animals of the National Institutes of Health. The experiments with human samples were approved by the Ethics Committees of the Tokyo Medical and Dental University (2011-22-3-1), of Tokyo Metropolitan Institute of Gerontology (2009-45) and of University of Tokyo (23-65-240413). The experiments using mice were approved by the Animal Experiments Committees of Tokyo Medical and Dental University (0130225A).

Database deposition

The mass spectrometry proteomics data have been deposited to the ProteomeXchange Consortium (82) via the PRIDE partner repository with the dataset identifier PXD001292.

SUPPLEMENTARY MATERIAL

Supplementary Material is available at *HMG* online.

ACKNOWLEDGEMENTS

We thank Drs Toshikazu Sasabe (TMDU), Tadafumi Hashimoto (Univ Tokyo) and Ms. Tayoko Tajima (TMDU) for technical support. We also thank PRIDE team for assistance to deposit our proteome data to the ProteomeXchange with identifier PXD001292.

Conflict of Interest statement. None declared.

FUNDING

This work was supported by the Strategic Research Program for Brain Sciences (SRPBS) and a Grant-in-Aid for Scientific Research on Innovative Areas (Foundation of Synapse and Neurocircuit Pathology) from the Ministry of Education, Culture, Sports, Science and Technology of Japan.

REFERENCES

1. Nukina, N. and Ihara, Y. (1985) Proteolytic fragments of Alzheimer's paired helical filaments. *J. Biochem.*, **98**, 1715–1718.
2. Grundke-Iqbal, I., Iqbal, K., Tung, Y.C., Quinlan, M., Wisniewski, H.M. and Binder, L.I. (1986) Abnormal phosphorylation of the microtubule-associated protein tau (tau) in Alzheimer cytoskeletal pathology. *Proc. Natl. Acad. Sci. USA*, **83**, 4913–4917.
3. Lee, V.M., Balin, B.J., Otvos, L. Jr and Trojanowski, J.Q. (1991) A68: a major subunit of paired helical filaments and derivatized forms of normal tau. *Science*, **251**, 675–678.
4. Masliah, E., Iimoto, D.S., Mallory, M., Albright, T., Hansen, L. and Saitoh, T. (1992) Casein kinase II alteration precedes tau accumulation in tangle formation. *Am. J. Pathol.*, **140**, 263–268.
5. Shoji, M., Iwakami, N., Takeuchi, S., Waragai, M., Suzuki, M., Kanazawa, I., Lippa, C.F., Ono, S. and Okazawa, H. (2000) JNK activation is associated with intracellular beta-amyloid accumulation. *Brain Res. Mol. Brain Res.*, **85**, 221–233.
6. Zhu, X., Ogawa, O., Wang, Y., Perry, G. and Smith, M.A. (2003) JKK1, an upstream activator of JNK/SAPK, is activated in Alzheimer's disease. *J. Neurochem.*, **85**, 87–93.
7. Takashima, A., Noguchi, K., Sato, K., Hoshino, T. and Imahori, K. (1993) Tau protein kinase I is essential for amyloid beta-protein-induced neurotoxicity. *Proc. Natl. Acad. Sci. USA*, **90**, 7789–7793.
8. Hanger, D.P., Byers, H.L., Wray, S., Leung, K.Y., Saxton, M.J., Seereeram, A., Reynolds, C.H., Ward, M.A. and Anderton, B.H. (2007) Novel phosphorylation sites in tau from Alzheimer brain support a role for casein kinase 1 in disease pathogenesis. *J. Biol. Chem.*, **282**, 23645–23654.
9. Wang, J.Z., Grundke-Iqbal, I. and Iqbal, K. (2007) Kinases and phosphatases and tau sites involved in Alzheimer neurofibrillary degeneration. *Eur. J. Neurosci.*, **25**, 59–68.
10. Piedrahita, D., Hernandez, I., Lopez-Tobon, A., Fedorov, D., Obara, B., Manjunath, B.S., Boudreau, R.L., Davidson, B., Laferla, F., Gallego-Gomez, J.C. *et al.* (2010) Silencing of CDK5 reduces neurofibrillary tangles in transgenic Alzheimer's mice. *J. Neurosci.*, **30**, 13966–13976.
11. Cleveland, D.W., Hwo, S.Y. and Kirschner, M.W. (1977) Purification of tau, a microtubule-associated protein that induces assembly of microtubules from purified tubulin. *J. Mol. Biol.*, **116**, 207–225.
12. Busciglio, J., Lorenzo, A., Yeh, J. and Yankner, B.A. (1995) Beta-amyloid fibrils induce tau phosphorylation and loss of microtubule binding. *Neuron*, **14**, 879–888.
13. Alonso, A.C., Zaidi, T., Grundke-Iqbal, I. and Iqbal, K. (1994) Role of abnormally phosphorylated tau in the breakdown of microtubules in Alzheimer disease. *Proc. Natl. Acad. Sci. USA*, **91**, 5562–5566.
14. Iqbal, K., Grundke-Iqbal, I., Zaidi, T., Merz, P.A., Wen, G.Y., Shaikh, S.S., Wisniewski, H.M., Alafuzoff, I. and Winblad, B. (1986) Defective brain microtubule assembly in Alzheimer's disease. *Lancet*, **2**, 421–426.
15. Roberson, E.D., Scearce-Levie, K., Palop, J.J., Yan, F., Cheng, I.H., Wu, T., Gerstein, H., Yu, G.Q. and Mucke, L. (2007) Reducing endogenous tau ameliorates amyloid beta-induced deficits in an Alzheimer's disease mouse model. *Science*, **316**, 750–754.
16. Mucke, L. and Selkoe, D.J. (2012) Neurotoxicity of amyloid beta-protein: synaptic and network dysfunction. *Cold Spring Harb. Perspect. Med.*, **2**, a006338.
17. Oka, T., Tagawa, K., Ito, H. and Okazawa, H. (2011) Dynamic changes of the phosphoproteome in postmortem mouse brains. *PLoS ONE*, **6**, e21405.
18. Mi, H., Lazareva-Ulitsky, B., Loo, R., Kejariwal, A., Vandergriff, J., Rabkin, S., Guo, N., Muruganujan, A., Doremieux, O., Campbell, M.J. *et al.* (2005) The PANTHER database of protein families, subfamilies, functions and pathways. *Nucleic Acids Res.*, **33**, D284–D288.
19. Leto, T.L., Fortugno-Erikson, D., Barton, D., Yang-Feng, T.L., Francke, U., Harris, A.S., Morrow, J.S., Marchesi, V.T. and Benz, E.J. Jr (1988) Comparison of nonerythroid alpha-spectrin genes reveals strict homology among diverse species. *Mol. Cell Biol.*, **8**, 1–9.
20. Bockers, T.M., Mameza, M.G., Kreutz, M.R., Bockmann, J., Weise, C., Buck, F., Richter, D., Gundelfinger, E.D. and Kreienkamp, H.J. (2001) Synaptic scaffolding proteins in rat brain. Ankyrin repeats of the multidomain shank protein family interact with the cytoskeletal protein alpha-fodrin. *J. Biol. Chem.*, **276**, 40104–40112.
21. Li, X. and Bennett, V. (1996) Identification of the spectrin subunit and domains required for formation of spectrin/adducin/actin complexes. *J. Biol. Chem.*, **271**, 15695–15702.
22. Matsuoka, Y., Li, X. and Bennett, V. (1998) Adducin is an in vivo substrate for protein kinase C: phosphorylation in the MARCKS-related domain inhibits activity in promoting spectrin-actin complexes and occurs in many cells, including dendritic spines of neurons. *J. Cell Biol.*, **142**, 485–497.
23. Pielage, J., Bulat, V., Zuchero, J.B., Fetter, R.D. and Davis, G.W. (2011) Hts/Adducin controls synaptic elaboration and elimination. *Neuron*, **69**, 1114–1131.
24. Hartwig, J.H., Thelen, M., Rosen, A., Janmey, P.A., Nairn, A.C. and Aderem, A. (1992) MARCKS is an actin filament crosslinking protein regulated by protein kinase C and calcium-calmodulin. *Nature*, **356**, 618–622.

25. Stumpo, D.J., Bock, C.B., Tuttle, J.S. and Blackshear, P.J. (1995) MARCKS deficiency in mice leads to abnormal brain development and perinatal death. *Proc. Natl. Acad. Sci. USA*, **92**, 944–948.
26. Bjorkblom, B., Padzik, A., Mohammad, H., Westerlund, N., Komulainen, E., Hollos, P., Parviainen, L., Papageorgiou, A.C., Iljin, K., Kallioniemi, O. *et al.* (2012) c-Jun N-terminal kinase phosphorylation of MARCKSL1 determines actin stability and migration in neurons and in cancer cells. *Mol. Cell Biol.*, **32**, 3513–3526.
27. Benowitz, L.I. and Routtenberg, A. (1997) GAP-43: an intrinsic determinant of neuronal development and plasticity. *Trends Neurosci.*, **20**, 84–91.
28. Gamby, C., Waage, M.C., Allen, R.G. and Baizer, L. (1996) Analysis of the role of calmodulin binding and sequestration in neuromodulin (GAP-43) function. *J. Biol. Chem.*, **271**, 26698–26705.
29. Routtenberg, A., Cantallops, I., Zaffuto, S., Serrano, P. and Namgung, U. (2000) Enhanced learning after genetic overexpression of a brain growth protein. *Proc. Natl. Acad. Sci. USA*, **97**, 7657–7662.
30. Mosevitsky, M.I., Capony, J.P., Skladchikova, G.Y., Novitskaya, V.A., Plekhanov, A.Y. and Zakharov, V.V. (1997) The BASP1 family of myristoylated proteins abundant in axonal termini. Primary structure analysis and physico-chemical properties. *Biochimie*, **79**, 373–384.
31. Laux, T., Fukami, K., Thelen, M., Golub, T., Frey, D. and Caroni, P. (2000) GAP43, MARCKS, and CAP23 modulate PI(4,5)P(2) at plasmalemmal rafts, and regulate cell cortex actin dynamics through a common mechanism. *J. Cell Biol.*, **149**, 1455–1472.
32. Schwarz, T.L. (2004) Synaptotagmin promotes both vesicle fusion and recycling. *Proc. Natl. Acad. Sci. USA*, **101**, 16401–16402.
33. Chen, L.T., Gilman, A.G. and Kozasa, T. (1999) A candidate target for G protein action in brain. *J. Biol. Chem.*, **274**, 26931–26938.
34. Blencowe, B.J., Issner, R., Nickerson, J.A. and Sharp, P.A. (1998) A coactivator of pre-mRNA splicing. *Genes Dev.*, **12**, 996–1009.
35. Ward, J.H.J. (1963) Hierarchical grouping to optimize an objective function. *J. Am. Stat. Assoc.*, **75**, 977–983.
36. Horn, H., Schoof, E.M., Kim, J., Robin, X., Miller, M.L., Diella, F., Palma, A., Cesareni, G., Jensen, L.J. and Linding, R. (2014) KinomeXplorer: an integrated platform for kinome biology studies. *Nat. Methods.*, **11**, 603–604.
37. Blom, N., Sicheritz-Pontén, T., Gupta, R., Gammeltoft, S. and Brunak, S. (2004) Prediction of post-translational glycosylation and phosphorylation of proteins from the amino acid sequence. *Proteomics*, **4**, 1633–1649.
38. Matus, A. (2000) Actin-based plasticity in dendritic spines. *Science*, **290**, 754–758.
39. Tada, T. and Sheng, M. (2006) Molecular mechanisms of dendritic spine morphogenesis. *Curr. Opin. Neurobiol.*, **16**, 95–101.
40. Palop, J.J. and Mucke, L. (2010) Amyloid-beta-induced neuronal dysfunction in alzheimer's disease: from synapses toward neural networks. *Nat. Neurosci.*, **13**, 812–818.
41. Wei, W., Nguyen, L.N., Kessels, H.W., Hagiwara, H., Sisodia, S. and Malinow, R. (2010) Amyloid beta from axons and dendrites reduces local spine number and plasticity. *Nat. Neurosci.*, **13**, 190–196.
42. Wu, H.Y., Hudry, E., Hashimoto, T., Kuchibhotla, K., Rozkalne, A., Fan, Z., Spires-Jones, T., Xie, H., Arbel-Ornath, M., Grosskreutz, C.L. *et al.* (2010) Amyloid beta induces the morphological neurodegenerative triad of spine loss, dendritic simplification, and neuritic dystrophies through calcineurin activation. *J. Neurosci.*, **30**, 2636–2649.
43. Ochman, A.R., Lipinski, C.A., Handler, J.A., Reaume, A.G. and Saporito, M.S. (2012) The lyn kinase activator MLR-1023 is a novel insulin receptor potentiator that elicits a rapid-onset and durable improvement in glucose homeostasis in animal models of type 2 diabetes. *J. Pharmacol. Exp. Ther.*, **342**, 23–32.
44. Craft, S. (2012) Alzheimer disease: insulin resistance and AD – extending the translational path. *Nat. Rev. Neurol.*, **8**, 360–362.
45. Fowler, V.M. and Adam, E.J. (1992) Spectrin redistributes to the cytosol and is phosphorylated during mitosis in cultured cells. *J. Cell Biol.*, **119**, 1559–1572.
46. Strittmatter, S.M., Fankhauser, C., Huang, P.L., Mashimo, H. and Fishman, M.C. (1995) Neuronal pathfinding is abnormal in mice lacking the neuronal growth cone protein GAP-43. *Cell*, **80**, 445–452.
47. Grasselli, G., Mandolesi, G., Strata, P. and Cesare, P. (2011) Impaired sprouting and axonal atrophy in cerebellar climbing fibres following in vivo silencing of the growth-associated protein GAP-43. *PLoS ONE*, **6**, e20791.
48. Abeliovich, A., Chen, C., Goda, Y., Silva, A.J., Stevens, C.F. and Tonegawa, S. (1993) Modified hippocampal long-term potentiation in PKC gamma-mutant mice. *Cell*, **75**, 1253–1262.
49. Abeliovich, A., Paylor, R., Chen, C., Kim, J.J., Wehner, J.M. and Tonegawa, S. (1993) PKC gamma mutant mice exhibit mild deficits in spatial and contextual learning. *Cell*, **75**, 1263–1271.
50. Orsini, C.A. and Maren, S. (2012) Neural and cellular mechanisms of fear and extinction memory formation. *Neurosci. Biobehav. Rev.*, **36**, 1773–1802.
51. Alkon, D.L., Sun, M.K. and Nelson, T.J. (2007) PKC signaling deficits: a mechanistic hypothesis for the origins of Alzheimer's disease. *Trends Pharmacol. Sci.*, **28**, 51–60.
52. Birnbaum, S.G., Yuan, P.X., Wang, M., Vijayraghavan, S., Bloom, A.K., Davis, D.J., Gobeske, K.T., Sweatt, J.D., Manji, H.K. and Arnsten, A.F. (2004) Protein kinase C overactivity impairs prefrontal cortical regulation of working memory. *Science*, **306**, 882–884.
53. Masliah, E., Cole, G.M., Hansen, L.A., Mallory, M., Albright, T., Terry, R.D. and Saitoh, T. (1991) Protein kinase C alteration is an early biochemical marker in Alzheimer's disease. *J. Neurosci.*, **11**, 2759–2767.
54. Clark, E.A., Leach, K.L., Trojanowski, J.Q. and Lee, V.M. (1991) Characterization and differential distribution of the three major human protein kinase C isozymes (PKC alpha, PKC beta, and PKC gamma) of the central nervous system in normal and Alzheimer's disease brains. *Lab. Invest.*, **64**, 35–44.
55. Etcheberrigaray, R., Tan, M., Dewachter, I., Kuiperi, C., Van der Auwera, I., Wera, S., Qiao, L., Bank, B., Nelson, T.J., Kozikowski, A.P. *et al.* (2004) Therapeutic effects of PKC activators in Alzheimer's disease transgenic mice. *Proc. Natl. Acad. Sci. USA*, **101**, 11141–11146.
56. Okamoto, K., Narayanan, R., Lee, S.H., Murata, K. and Hayashi, Y. (2007) The role of CaMKII as an F-actin-bundling protein crucial for maintenance of dendritic spine structure. *Proc. Natl. Acad. Sci. USA*, **104**, 6418–6423.
57. Lee, S.J., Escobedo-Lozoya, Y., Szatmari, E.M. and Yasuda, R. (2009) Activation of CaMKII in single dendritic spines during long-term potentiation. *Nature*, **458**, 299–304.
58. Muller, G., Wied, S. and Frick, W. (2000) Cross talk of pp125(FAK) and pp59(lyn) non-receptor tyrosine kinases to insulin-mimetic signaling in adipocytes. *Mol. Cell. Biol.*, **20**, 4708–4723.
59. Shehadeh, L.A., Yu, K., Wang, L., Guevara, A., Singer, C., Vance, J. and Papapetropoulos, S. (2010) SRRM2, a potential blood biomarker revealing high alternative splicing in Parkinson's disease. *PLoS ONE*, **5**, e9104.
60. Genoux, D., Haditsch, U., Knobloch, M., Michalon, A., Storm, D. and Mansuy, I.M. (2002) Protein phosphatase 1 is a molecular constraint on learning and memory. *Nature*, **418**, 970–975.
61. Wu, P., Zhao, Y., Haidacher, S.J., Wang, E., Parsley, M.O., Gao, J., Sadygov, R.G., Starkey, J.M., Luxon, B.A., Spratt, H. *et al.* (2013) Detection of structural and metabolic changes in traumatically injured hippocampus by quantitative differential proteomics. *J. Neurotrauma*, **30**, 775–788.
62. Chu, S. and Ferro, T.J. (2006) Identification of a hydrogen peroxide-induced PP1-JNK1-Sp1 signaling pathway for gene regulation. *Am. J. Physiol. Lung Cell Mol. Physiol.*, **291**, L983–L992.
63. Comi, C., Carecchio, M., Chiocchetti, A., Nicola, S., Galimberti, D., Fenoglio, C., Cappellano, G., Monaco, F., Scarpini, E. and Dianzani, U. (2010) Osteopontin is increased in the cerebrospinal fluid of patients with Alzheimer's disease and its levels correlate with cognitive decline. *J. Alzheimers Dis.*, **19**, 1143–1148.
64. Simonsen, A.H., McGuire, J., Podust, V.N., Davies, H., Minthon, L., Skoog, I., Andreasen, N., Wallin, A., Waldemar, G. and Blennow, K. (2008) Identification of a novel panel of cerebrospinal fluid biomarkers for Alzheimer's disease. *Neurobiol. Aging*, **29**, 961–968.
65. Weber, G.F., Zawaideh, S., Hikita, S., Kumar, V.A., Cantor, H. and Ashkar, S. (2002) Phosphorylation-dependent interaction of osteopontin with its receptors regulates macrophage migration and activation. *J. Leukoc. Biol.*, **72**, 752–761.
66. Jono, S., Peinado, C. and Giachelli, C.M. (2000) Phosphorylation of osteopontin is required for inhibition of vascular smooth muscle cell calcification. *J. Biol. Chem.*, **275**, 20197–20203.
67. Ahmed, M. and Kundu, G.C. (2010) Osteopontin selectively regulates p70S6K/mTOR phosphorylation leading to NF-kappaB dependent AP-1-mediated ICAM-1 expression in breast cancer cells. *Mol. Cancer*, **9**, 101.
68. Watabe-Rudolph, M., Song, Z., Lausser, L., Schnack, C., Begus-Nahrmann, Y., Scheithauer, M.O., Rettinger, G., Otto, M., Tumani, H., Thal, D.R. *et al.* (2012) Chitinase enzyme activity in CSF is a powerful biomarker of Alzheimer disease. *Neurology*, **78**, 569–577.

69. Jankowsky, J.L., Fadale, D.J., Anderson, J., Xu, G.M., Gonzales, V., Jenkins, N.A., Copeland, N.G., Lee, M.K., Younkin, L.H., Wagner, S.L. *et al.* (2004) Mutant presenilins specifically elevate the levels of the 42 residue beta-amyloid peptide in vivo: evidence for augmentation of a 42-specific gamma secretase. *Hum. Mol. Genet.*, **13**, 159–170.
70. Oyama, F., Sawamura, N., Kobayashi, K., Morishima-Kawashima, M., Kuramochi, T., Ito, M., Tomita, T., Maruyama, K., Saido, T.C., Iwatsubo, T. *et al.* (1998) Mutant presenilin 2 transgenic mouse: effect on an age-dependent increase of amyloid beta-protein 42 in the brain. *J. Neurochem.*, **71**, 313–322.
71. Hsiao, K., Chapman, P., Nilsen, S., Eckman, C., Harigaya, Y., Younkin, S., Yang, F. and Cole, G. (1996) Correlative memory deficits, Abeta elevation, and amyloid plaques in transgenic mice. *Science*, **274**, 99–102.
72. Oakley, H., Cole, S.L., Logan, S., Maus, E., Shao, P., Craft, J., Guillozet-Bongaarts, A., Ohno, M., Disterhoft, J., Van Eldik, L. *et al.* (2006) Intraneuronal beta-amyloid aggregates, neurodegeneration, and neuron loss in transgenic mice with five familial alzheimer's disease mutations: potential factors in amyloid plaque formation. *J. Neurosci.*, **26**, 10129–10140.
73. Yoshiyama, Y., Higuchi, M., Zhang, B., Huang, S.M., Iwata, N., Saido, T.C., Maeda, J., Suhara, T., Trojanowski, J.Q. and Lee, V.M. (2007) Synapse loss and microglial activation precede tangles in a P301S tauopathy mouse model. *Neuron*, **53**, 337–351.
74. Shilov, I.V., Seymour, S.L., Patel, A.A., Loboda, A., Tang, W.H., Keating, S.P., Hunter, C.L., Nuwaysir, L.M. and Schaeffer, D.A. (2007) The paragon algorithm, a next generation search engine that uses sequence temperature values and feature probabilities to identify peptides from tandem mass spectra. *Mol. Cell Proteomics*, **6**, 1638–1655.
75. Elias, J.E. and Gygi, S.P. (2007) Target-decoy search strategy for increased confidence in large-scale protein identifications by mass spectrometry. *Nat. Methods*, **4**, 207–214.
76. Nagasaki, M., Doi, A., Matsuno, H. and Miyano, S. (2003) Genomic object net: I. A platform for modelling and simulating biopathways. *Appl. Bioinforma.*, **2**, 181–184.
77. Yang, G., Pan, F., Parkhurst, C.N., Grutzendler, J. and Gan, W.B. (2010) Thinned-skull cranial window technique for long-term imaging of the cortex in live mice. *Nat. Protoc.*, **5**, 201–208.
78. Yan, Z., Feng, J., Fienberg, A.A. and Greengard, P. (1999) D(2) dopamine receptors induce mitogen-activated protein kinase and cAMP response element-binding protein phosphorylation in neurons. *Proc. Natl. Acad. Sci. USA*, **96**, 11607–11612.
79. Saporito, M.S., Ochman, A.R., Lipinski, C.A., Handler, J.A. and Reaume, A.G. (2012) MLR-1023 is a potent and selective allosteric activator of lyn kinase in vitro that improves glucose tolerance in vivo. *J. Pharmacol. Exp. Ther.*, **342**, 15–22.
80. Galan, A., Laird, J.M. and Cervero, F. (2004) In vivo recruitment by painful stimuli of AMPA receptor subunits to the plasma membrane of spinal cord neurons. *Pain*, **112**, 315–323.
81. Gillet, L.C., Navarro, P., Tate, S., Rost, H., Selevsek, N., Reiter, L., Bonner, R. and Aebersold, R. (2012) Targeted data extraction of the MS/MS spectra generated by data-independent acquisition: a new concept for consistent and accurate proteome analysis. *Mol. Cell Proteomics*, **11**, 1–17.
82. Vizcaíno, J.A., Deutsch, E.W., Wang, R., Csordas, A., Reisinger, F., Ríos, D., Dianes, J.A., Sun, Z., Farrah, T., Bandeira, N. *et al.* (2014) ProteomeXchange provides globally co-ordinated proteomics data submission and dissemination. *Nat. Biotechnol.*, **30**, 223–226.